Sources of Concentric Gravity Waves Generated by a Moving Mesoscale Convective System in Southern Brazil

Prosper Kwamla Nyassor[1], Cristiano Max Wrasse[1], Igo Paulino[2], Eliah F. M. T. São Sabbas[3], José Valentine Bageston[4], Kleber Pinheiro Naccarato[5], Delano Gobbi[1], Cosme Alexandre Oliveira Barros Figueiredo[1], Toyese Tunde Ayorinde[1], Hisao Takahashi[1], and Diego Barros[1]

[1]Space Weather Division, National Institute for Space Research (INPE), São José dos Campos, SP, Brazil
[2]Department of Physics, Federal University of Campina Grande (UFCG), Campina Grande, PB, Brazil
[3]Heliophysics, Planetary Science and Aeronomy Division, INPE, São José dos Campos, SP, Brazil
[4]Southern Space Coordination, Santa Maria, National Institute for Space Research, RS, Brazil
[5]Impacts, Adaptation and Vulnerabilities Division, INPE, São José dos Campos, SP, Brazil

Correspondence: Prosper Kwamla Nyassor (prosper.nyassor@inpe.br)

Abstract. The studies on the sources of three concentric gravity waves (CGWs) excited by a moving Mesoscale Convective System (MCS) on the night of October 1 - 2, 2019 are investigated. These CGWs were observed using an OH all-sky imager whereas the MCS were observed by the Geostationary Operational Environmental Satellite (GOES). Using 2D spectral analysis, we observed that the CGWs have horizontal wavelength λ_H ∼30 - 55 km, phase speed c_H ∼70 - 90 m/s, and period τ

5 ∼7 - 12 min. By backward ray tracing we found that two of the waves were excited from convective cores within the MCS. We also found that the epicenters of the CGWs were close to the tropopause positions of the ray traced paths as well as the nearby convective cores. Regarding the source, we verified that on this night the cold-point tropopause (CPT) was ∼-80°C, which was ∼10°C cooler than CPT on the days preceding and after the MCS, and also colder than usually observed. Since the tropopause height and temperature are fundamental parameters underlying the analysis of the overshooting extent, we developed our own

10 methodology to establish a reference tropopause that would enable a quantitative estimate of this parameter. Since the MCS (CGWs source) was moving, the overshooting convective cores were tracked in space and time. Finally, we found that two out of the three CGWs were excited by the MCS whereas the source of the remaining one was found not to be directly associated with the MCS.

15 ## 1 Introduction

Atmospheric gravity waves (AGWs or simply GWs) play a vital role in the dynamics and thermodynamics of the middle (Fritts and Alexander, 2003) and upper atmosphere (Yiğit et al., 2021). GWs are excited when a disturbance is introduced between stable layers of the atmosphere by either buoyancy (Gossard and Hooke, 1975) or gravity (Nappo, 2013). During the propagation of the generated GWs from the lower to upper atmosphere, the energy and momentum released to excite the

20 GWs are transported by the waves. This energy and momentum are deposited in the middle and upper atmosphere during the dissipation of GWs, thus contributing turbulence and mixing, and influencing the mean circulation and thermal structure of the middle and upper atmosphere (Fritts and Alexander, 2003; Yiğit and Medvedev, 2009).

   There are several known sources of the GWs among which tropospheric convection - severe weather conditions such as thunderstorms are considered to be the most important and natural sources of AGWs in the troposphere. Tropospheric con-
25 vection has three main GWs generation mechanisms, that is, pure thermal forcing, "obstacle" or "transient mountain" effect, and "mechanical oscillator". Among these three, the mechanical oscillator (overshooting) mechanism is known to be one of the natural sources of concentric gravity waves (CGWs). Most tropospheric deep convection - CGWs cases in literature has other associated convection related phenomena, such as hailstorm (Yue et al., 2009; Vadas et al., 2012), lightning (Yue et al., 2014; Nyassor et al., 2021) and Transient Luminous Events (TLEs) (Boccippio et al., 1995; São Sabbas and Sentman, 2003;
30 Sentman et al., 2003; Pasko et al., 2012) which are used as a measure of the severity of the thunderstorm. The relationship between CGWs and deep convection have been established using observations (Yue et al., 2009) and in some cases observation complemented by numerical studies (Vadas et al., 2009b, 2012; Nyassor et al., 2021).

   Observations of CGWs are made using ground-based instruments, such as all-sky imagers that capture GWs activities in the mesosphere in 2 dimensions. (Sentman et al., 2003; Yue et al., 2009, 2013; Vadas et al., 2012; Nyassor et al., 2021). Satellite
35 imaging data from Atmospheric Infrared Sounder (AIRS), Visible Infrared Imaging Radiometer Suite (VIIRS), have also been used to study GWs/CGWs activities in the stratosphere and mesopause region, respectively (Wen et al., 2018; Yue et al., 2014). Regarding the observation of tropospheric convective sources of GWs/CGWs, infrared images of cloud top brightness temperatures (CTBT) from satellite imagery has been used (Vadas et al., 2009a; Yue et al., 2009; Azeem et al., 2015; Takahashi et al., 2018; Figueiredo et al., 2018; Nyassor et al., 2021). In most of the reported works on observation of CGWs and deep
40 convection, CTBT images showed overshooting of the tropopause by 1 - 3 km prior to observation of the CGWs (Yue et al., 2009, 2014; Nyassor et al., 2021). Similar works by Vadas et al. (2009a), Vadas et al. (2012), Xu et al. (2015) and Nyassor et al. (2021) used ray tracing model to relate observed CGWs in OH emission altitude ∼87 km to overshooting top in CTBT images captured by the Geostationary Operational Environmental Satellites (GOES). Also, recent observational and simulation studies (e.g., Lane et al., 2001; Vadas et al., 2009b; Nyassor et al., 2021) have established a direct relationship between some
45 parameters of observed GWs and some parameters of their respective sources.

   Using observational data, Nyassor et al. (2021) established a direct relationship between the period of the observed mesospheric CGWs and the periods of the sources (thunderstorms) using lightning data. They conducted case studies on three CGWs events observed in São Martinho da Serra, where the data for this current work was also collected. The sources of the CGWs studied were identified to be excited by nearby deep convective cores in thunderstorms using backward ray tracing and the
50 geometric determined center. A time series CTBT image of the identified source revealed that the entire deep convection was not moving but evolving with time in size. The overshooting tops of the convective cores within these deep convection were estimated and found to overshot vertically upward into the stratosphere by ∼1 - 1.5 km. Using the spatial distribution of the lightning densities (obtained by binning the lightning strike in $0.06° \times 0.06°$ grid boxes), the regions with high lightning den-

sities agree with the regions with the coldest cloud top brightness temperature. Using the lightning flash rate, the periodicities
55 in the variations of the updraft/overshooting oscillations were estimated and compared to the CGWs periods.

In this current study, we investigated the sources of CGWs excited from the troposphere by a convective overshooting
mechanism in the OH emission excited by a moving Mesoscale Convective System (MCS) on the night of October 1 - 2,
2019 at São Martinho da Serra (29.48°S, 53.87°W). We also report two of the Transient Luminous Events (TLEs) observed
during the CGW events this night, two groups of sprites, excited in upper atmosphere above the MCS by its lighting activity.
60 Similar methodologies used by Nyassor et al. (2021) were employed here except for the effect of the MCS on the tropopause
and the resultant estimated overshooting tops. The influence of the MCS on the tropopause temperature will be studied by
considering days with and without convective activity including the day of the CGWs event to estimate the actual tropopause
temperature since its presence appears to further decrease the tropopause temperature. Since the source (MCS), as well as the
convective regions, were moving and evolving at the same time, the overshooting convective cores were tracked in space and
65 time to identify the most likely cores that overshot to excite the observed CGWs. Finally, using the CGWs parameters and the
dispersion relation, the horizontal wavelength spectra above the tropopause were estimated over the region the CGWs were
observed. These estimated horizontal wavelength spectra above the tropopause were compared to the observed wavelengths in
the OH emission layer.

2 Observation and Methodology

70 The OH all-sky imager installed at the Southern Space Observatory (SSO) by the National Institute for Space Research (INPE)
and coordinated by the Southern Space Coordination (COESU/INPE) at São Martinho da Serra (SMS) located at 29.44°S,
53.82°W, altitude 488.7 m in the Southern part of Brazil was used to observe and study the CGWs. The imager has a single
three inches OH-NIR optical filter with a notch at 865.5 nm. Each image has an integration time of ∼20 seconds with a
sampling rate of ∼38 seconds. The original image was cropped from 1024×1024 pixels to 512×512. The camera used is a
75 low-cost front-illuminated Charged Coupled Device (CCD) with a chip size of 24.5×24.5 mm and a pixel array of 1024×1024
pixels. The CCD uses a 2 stage thermoelectric air cooling system, which provides 40°C below ambient temperature. Further
information on this airglow imager can be found in Bageston et al. (2009) and Nyassor et al. (2021).

The observatory also hosts one of the eight TLE observation stations of the Transient Luminous Event and Thunderstorm
High Energy Emission Collaborative Network (LEONA). The LEONA TLE stations are installed at different locations in
80 Brazil and Argentina, covering the whole region of Uruguay, Paraguay, Northeastern Argentina, Southern Brazil and part of
Central Brazil. LEONA also has one mobile High Energy Emission Thunderstorm (HEET) station composed of a neutron
detector that is normally installed at INPE headquarters in São José dos Campos, but can be moved to be installed anywhere
during a field campaign. The TLE station at the SSO, with which the two sprites events reported here were observed, is
composed of two Watec low-light video cameras fitted with lenses that yield fields of view of ∼20 - 30° and have a previously
85 verified observation range of ∼1100 km into Argentina, Uruguay and Paraguay (São Sabbas et al., 2010). The cameras are

monochromatic with sensitivity in the visible and near-IR wavelengths and are remotely operated in real time during the observations. More information about the LEONA Network can be found in São Sabbas et al. (2019).

The CTBT captured in channel 13, 10.3 μm infrared (IR) images from the Geostationary Operational Environmental Satellite 16 (GOES-16), provided by the Brazilian Center for Weather Forecast and Climate Studies (CPTEC/INPE) was used to observe and study the MCS activities during the CGW events. The images are taken every 10 min with each pixel corresponding to approximately 2 km at the equator. Radiosonde and radio occultation data were used to study the atmospheric vertical temperature profile. Also, associated MCS lightning activities were observed using the Brazilian Lightning Detection Network (BrasilDAT) sensors (Naccarato and Pinto, 2009, 2012; Nyassor et al., 2021).

On October 2, 2019, the SMS OH imager observed curved-like structures emanating from the southwestern part of the observatory between the hours of 00:13 UT and 04:15 UT. After employing the image preprocessing technique of Garcia et al. (1997) and Wrasse et al. (2007), the unwarped images showed three different concentric structures with different epicenters at separate times. Samples of the unwarped images for each of the observed concentric structures are shown in Figure 1. The red rectangles denote the regions where the concentric structures are seen on the OH image. The white triangle indicates the center of the image as well as the location of the observation site.
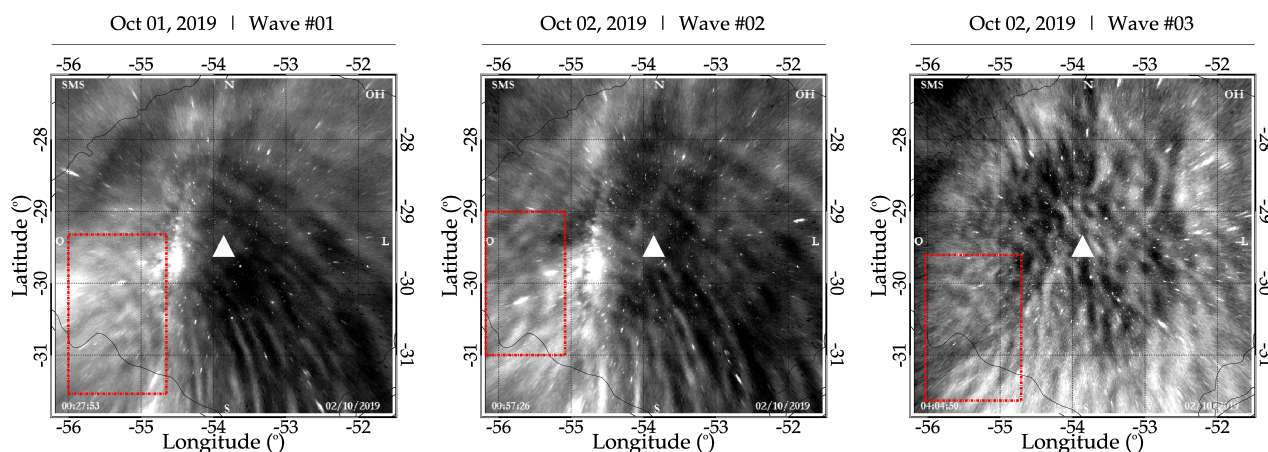
Figure 1. Example of unwarped images of each of the concentric gravity wave (CGWs) event observed at São Martinho da Serra on October 1 - 2, 2019. On the left is Wave #01 at 00:27 UT, in the middle is Wave #02 at 00:57 UT, and on the right is Wave #03 at 04:04 UT. The white triangle shows the center of the image (which is also the location of the SMS observatory) and the red rectangles show the regions of the CGWs events.

The time at which the CGWs were first identified, their estimated centers in latitude, longitude, and the CGWs parameters are summarized in Table 1. The appearance of the concentric structures in the airglow indicates; 1) the point-like convective overshooting of the tropopause by 1 - 3 km into the stratosphere (Vadas and Fritts, 2009; Vadas et al., 2009b; Yue et al., 2009) and 2) weak intervening background wind (Yue et al., 2009; Vadas and Fritts, 2009).

Table 1. Parameters of Excited Waves during the October 1 – 2, 2019 CGW Events

Wave Parameters		Wave #01	Wave #02	Wave #03
Obs. Time (UT)		00:27:53	00:55:56	04:04:50
λ_H (km)		50.30±04.60	54.90±05.00	30.50±04.10
c_H (m/s)		73.90±10.60	91.00±09.00	72.90±08.60
τ (min)		11.40±01.90	10.00±03.00	07.00±00.80
ϕ (°)		31.60	90.00	89.50
CGWs Center	Lon	55.0°W	55.5°W	55.9°W
	Lat	30.8°W	29.29°W	30.9°W
CGWs Radius (km)		154.21	139.23	119.40

The wave parameters: horizontal wavelength (λ_H), observed period (τ), horizontal phase speed (c_H), and propagation di-
rection (ϕ)) of the observed CGWs in the airglow images, were extracted using a two-dimensional spectral analysis technique
(Garcia et al., 1997; Wrasse et al., 2007). Due to the annular nature of CGWs, the wave parameters were estimated for three
different directions extending from the center of the CGW. For each direction, the wave parameters were obtained assuming
a plane wave locally. Average values of the parameters of the three directions were computed. The three directions were con-
sidered in order to verify that the observed CGWs emanated from the same point source (Nyassor et al., 2021). The average
values of the wave parameters are presented in Table 1. To study the propagation of the CGWs and determine their possible
sources locations, the geometrically determined center and backward ray tracing were used.

2.1 Determination of Source of the Observed Waves

Two different methods were used to identify the possible source positions of the CGWs. The first method was the determination
of the geometric center of the CGWs which is a zeroth-order approximation of the source location following the approach of
Pedoe (1995) and Nyassor et al. (2021). The description of the methodology used to determine the center of the CGWs (in this
description a circle with unknown center and radius) is as follows with the accompanying pictorial description shown in Figure
2. It is important to mention that this method can be used to determine the center of arc-like and circular GWs. To determine
the CGW center geometrically:

1. a circle with assumed center and radius is drawn as shown in panel (a) of Figure 2;

2. three circles (panels (b), (c), and (d)) with similar radii were constructed on the circumference of the circle in (a) (in the
   case of CGW, the circumference can be either the first crest or trough of the visible concentric ring on the OH image);

3. two intersecting lines were constructed through the intersection points of the first two adjacent circles (panel (e)) and the
   second two adjacent circles (panel (f));

4. the center of the circle (CGWs) with an unknown center is then determined as the intersection point (P) of the two
125   intersecting lines as shown in panel (g) in Figure 2;

5. finally, to determine the radius of the circle (CGW), a right-angle triangle was constructed using the center (i.e., P) and
   any two centers (which can be points Q and R or R and S) of the three circles drawn on the circumference (for CGW,
   the concentric crest or trough). The light-grey triangular shaded region emphasizes $\triangle QPR$, whereas the grey shaded
   triangular region emphasizes $\triangle RPS$. Using any of these triangles, the radius can be computed.
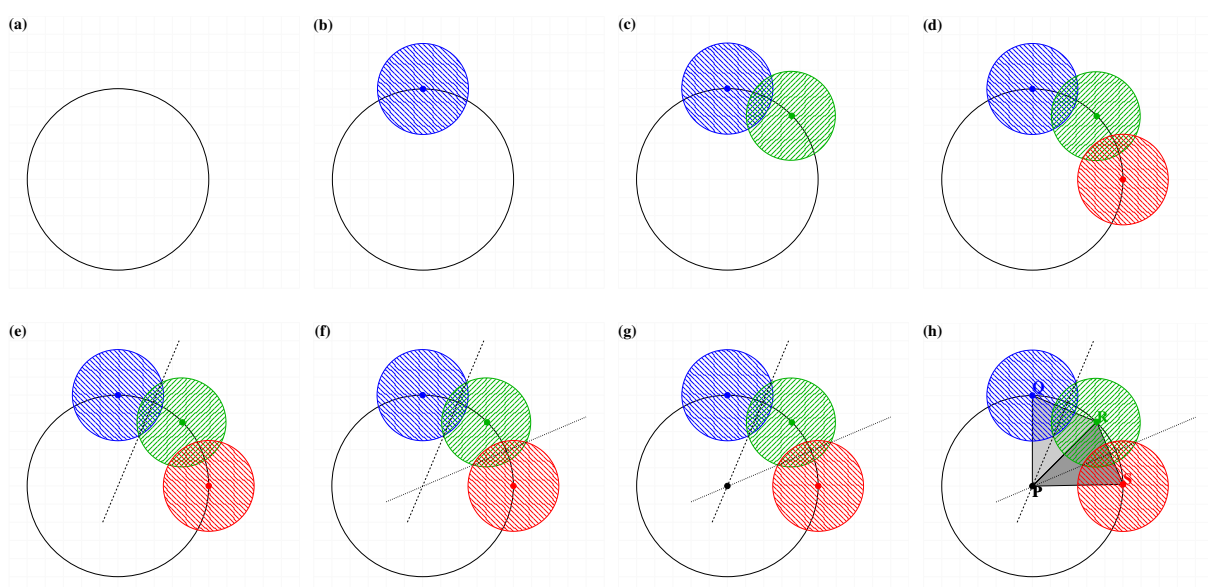
Figure 2. Step by step description of the determination of the center of a CGW using a circle with an assumed unknown center and radius.

130   The second method to determine the source location employs the use of the ray tracing model. The model utilized in this
work follows the approach of Vadas (2007) which incorporates the kinematic viscosity and thermal diffusivity. To determine
the next ray point in space and time, the Equations:

$$\frac{dx_i}{dt} = V_i + \frac{\partial \omega_{Ir}}{\partial k_i} = V_i + c_{g_i} \tag{1}$$

and

$$\frac{dk_i}{dt} = -k_j \frac{\partial V_j}{\partial x_i} - \frac{\partial \omega_{Ir}}{\partial x_i} \tag{2}$$

were solved numerically using the fourth-order Runge-Kutta routine Press et al. (2007). The indices; i, j = 1, 2, 3 indicate the
components of vector quantities; position (x), velocity (V), wavenumber (k), and the group velocity c_g. The initial position and

time where and when the ray tracing began was the location of the first visible concentric crest or trough in the OH emission layer altitude, that is, $p_i = (lon_i; lat_i; alt_i; t_i)$.

140   The gravity wave parameters, the backgrounds, that is, the wind from the MERRA-2 reanalysis (e.g., Gelaro et al., 2017) and HWM-14 (e.g., Drob et al., 2015), temperature from MERRA-2, and NRLMSISE-00 (e.g., Picone et al., 2002) models were used as the input parameters. Due to the altitude limitation of the MERRA-2 wind and temperature, MERRA-2 wind and temperature profiles were merged (concatenated) with HWM-14 and NRLMSISE-00 profiles, respectively. The backgrounds (i.e., wind and temperature) were concatenated within 65 - 75 km of altitude.

145   The concatenation was done to attain the altitude range from $0 - 100$ km since MERRA-2 wind and temperature extends up to 75 km. To minimize any discontinuities at the altitude of concatenation, an altitude range of 65 - 75 km was set for the MERRA-2 and HWM14 winds. The difference between the two winds at each kilometer within the set range was computed. Then, the altitude with the smallest difference is chosen as the concatenation altitude. This makes the concatenated altitude vary between the set range for each wind profile. Finally, the concatenated profile was smooth at each three points. A similar procedure is
150   also used to concatenate the MERRA-2 and NRLMSISE-00 temperatures. Since MERRA-2 has a temporal resolution of 3 h, interpolation was performed for each time step (Nyassor et al., 2021). To perform the iteration for the next step, the following stopping conditions were defined:

1. the group velocity should be less than or equal to 0.9 times the speed of sound ($c_g \leq 0.9 C_s$)

2. the real component of the intrinsic frequency must be greater than zero ($\omega_{Ir} > 0$)

155   3. the momentum flux at all points of the wave trajectory must satisfy the expression: $R_m > 10^{-15} R_0$, where R_m is the momentum flux at each altitude and R_0 is the momentum flux at the reference altitude. The factor 10^{-15} was arbitrarily chosen

4. the module of the vertical wavelength must be less than viscosity scale $\left[|\lambda_z| < \frac{2\pi}{\frac{d\nu/dz}{\nu}} \right]$. Here, $\nu = \frac{\mu}{\rho}$ is kinematic viscosity with μ being molecular viscosity and ρ the density (Vadas, 2007)

160   Note that the items (3) and (4) are important when forward ray tracing the waves into the thermosphere.

2.2   Determination of tropopause temperature and altitude, and overshooting tops

Usually, the tropopause is determined using either the lapse rate (Xian and Homeyer, 2019) or cold-point (Kim and Son, 2012) criteria. In this work, both criteria were used because the tropopause temperature during the night of the CGWs events was colder than what was usually reported in literature. Therefore, the days before and after the night of the CGWs events were
165   considered in order to investigate the impact of the MCS on the tropopause. Some studies (e.g., Sherwood et al., 2003; Kim et al., 2018) suggest that extreme active deep convection appears to cool the layer near the cloud top thereby causing colder tropopause. On this basis data from radiosonde and radio occultation soundings near/around the observation site and the MCS were used to study the effect of the MCS on the tropopause.

The variation in the tropopause height and temperature of the radiosonde measurement were verified using temperature

170 profile from radio occultation. The radio occultation temperature profiles obtained between October 1 to October 3, 2019 to verify the behavior of the tropopause height and temperature variation are shown in Figure A1 of Appendix A. Using the radio occultation temperature profiles, the vertical wavelengths from altitudes 10 - 50 km were estimated. A continuous wavelet transform (CWT) (Torrence and Compo, 1998) was used to decompose the temperature profile to obtain the temperature fluctuation. The CWT was applied on the temperature fluctuation profile between the scale of 4 - 30 km to obtain the required

175 range of vertical wavelength of interest.

To quantitatively estimate the vertical extension of the overshooting tops, it is important to first properly determine the tropopause temperature and altitude. So, the colder the tropopause, the more energetic the convection needs to be to produce overshooting into the stratosphere. The observation of these three CGWs indicates convective overshooting of the tropopause by at least ~1 - 3 km, the criteria for convection to generate GWs, which is considered to be the main mechanism to generate

180 CGWs (Yue et al., 2009; Vadas et al., 2009b, 2012; Nyassor et al., 2021). Two distinct estimation methods of the overshooting tops were used in this work and their results were compared: (i) the adopted approach of Griffin et al. (2016) in Nyassor et al. (2021), and (ii) a simplified version of the method of São Sabbas et al. (2009).

The first approach is an approximation in which the tropopause temperature and altitude are obtained taken from the radiosonde temperature profile. For this approach, the tropopause is taken to be the first temperature inversion point. This in-

185 version point was estimated following the definition of the World Meteorological Organization standard (Xian and Homeyer, 2019). Adapting Equation 3, the overshooting top height (OT_{Height}) from Griffin et al. (2016), the overshooting tops (OT) were estimated using the brightness temperature (BT) of the OT, the tropopause height and temperature. The cloud top brightness temperature was obtain from the Advanced Baseline Imager (ABI), which is an imaging radiometer of GOES-R satellite. The ABI has 16 different spectral bands, including two visible channels, four near-infrared channels, and 10 infrared channels

190 with a spatial resolution of 0.5-2 km. Among the weather and climate products of these channels, the CTBT product is derived from the 11, 12 and 13.3 μm infrared observations.

$$OT_{Height} = H_{Trop} + \frac{OT_{BT} - T_{Trop}}{OT_{LR}}, \tag{3}$$

Here H_{Trop} is the tropopause height, OT_{BT} is the brightness temperature of the OT, T_{Trop} is the tropopause temperature and OT_{LR} is the OT lapse rate. The OT lapse rate was estimated using the radiosonde profile and the CTBT. The OT lapse rate

195 for the days considered in the determination of the tropopause temperature and altitude were averaged and was found to be -7.35 Kkm^{-1}.

In the second method to identify the convective cores of a given convective region, we calculated the average temperature ($\overline{T}$) of the coldest cloud tops and their surroundings (São Sabbas et al., 2009, 2010). To calculate the $\overline{T}$, we added the temperature of all pixels whose values were lower than a threshold. This threshold is defined as T ≤ -70°C. Next, the sum of the temperature

200 lower than the threshold was divided by the total number of pixels. We then calculated the difference between the temperature of the pixel and the average, that is, $\Delta T = T_{pixel} - \overline{T}$. The averaging was performed within a spatial grid of 10×10 km and a

temporal range within 10 minutes. The pixels with the lowest ΔT were selected as the "center" of the convective cores (T_{core}) and their area was estimated by adding the area of surrounding pixels until $\Delta T = T_{core}/2$. In most cases, the temperature gradient around the convective core center was rather sharp, the number of pixels with $\Delta T \leq T_{core}/2$ was small, and all of them were included. For the few convective cores that extended to larger areas and/or merged with other convective cores, only a few pixels outward in each direction from the coldest spot were included. We also estimated the tropopause overshoot of the convective cores by subtracting the altitude of the convective core, obtained making a simple comparison between T_{core} (which is the coldest region of the CTBT) and the Tropopause altitude were obtained from the radiosonde soundings (Adler and Fenn, 1979; Heymsfield and Blackmer Jr, 1988).

3 Results and Discussions

3.1 Ray Tracing Results of the CGWs

The ray tracing results of the three CGWs are presented in Figures 3, 4, and 5 for Waves #01, #02, and #03, respectively. Panels (a) of these figures show the longitudinal and latitudinal variations of the ray path for the individual CGW events. The time-altitude variations of the three CGW events are shown in panels (b). The color bars above each plot show the temperature scale of the IR CTBT. The zoom-in region without the CTBT is used to show the trajectory of the OTs in space around the determined center and the tropopause position of the ray paths. The squares (dark red and orange) and the circles (red and black) in the zoom-in region indicate the spatial distribution of the OTs. The times when these waves were first identified on the airglow images are presented in Table 1.

The IR cloud top brightness temperatures plotted reflect the status of the MCS closet to the time when the CGW ray path reached the tropopause, which is considered to be the excitation altitude. The coldest regions has been used to identify convective overshooting tops (Bedka et al., 2010; Jurković et al., 2015) and the possible source of the CGWs (Yue et al., 2009; Vadas and Liu, 2009; Yue et al., 2014; Azeem et al., 2015; Xu et al., 2015; Nyassor et al., 2021). The altitudes from which the ray tracing began, that is, ∼87 km, (the OH emission layer) is denoted by the black dotted line in panel (b) of Figures 3, 4, and 5 whereas in the same figures the altitudes of the tropopause obtained from the radiosonde measurement are the black dashed line. A similar cloud top brightness temperature plots with extended longitude and latitude ranges of panels (a) of Figures 3, 4, and 5 have been attached in the Appendix B to show a larger view of the MCS around the CGWs. Figures 3a, 4a, and 5a are Figures B1, B2, and B3, respectively with only the first visible concentric crest and their centers plotted over the map to give an idea about the position of the waves.

3.2 Effect of Background Wind on the Wave Event

A blocking diagram described by Medeiros et al. (2003),Giongo et al. (2020), and Nyassor et al. (2021) adapted from Taylor et al. (1993) was employed to study the state of the background wind relative to the wave. The blocking diagram consid-
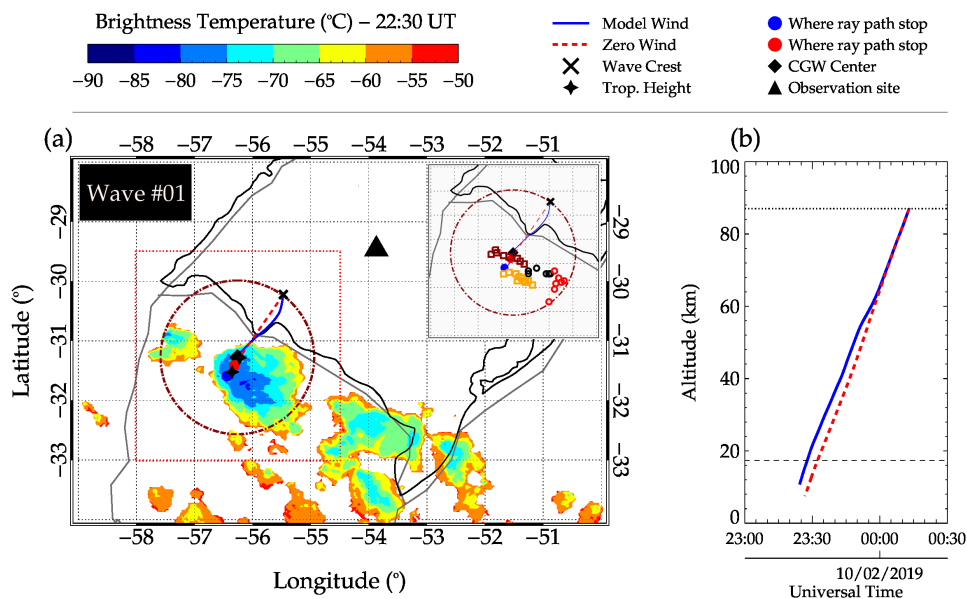
Figure 3. Ray tracing results of concentric gravity waves (CGWs) event one (#01) on October 1 - 2, 2019. In (a), the individual path of the wave trajectory of the CGW and the MCS at the time the ray path reached the tropopause are presented. The wave crest, tropopause height, observation site, CGW center (of the dotted-dashed circle), and the stopping points of each ray path are represented by the symbols; cross, star, triangle, diamond, blue-filled, and red-filled circles, respectively. The time-altitude profile of the ray path is shown in (b). In both panels, the blue solid lines denote the ray path of the wave trajectory using the model wind (i.e., MERRA-2 and HWM14), whereas the red dashed lines represent the ray paths of wave trajectory where zero wind was considered. In the zoom-in region in the upper-right corner of (a) which is depicted by the red-dotted square, the open squares and open circles indicate the positions of the convective cores. The OTs (convective cores (C)); #1, #2, #3, and #4 are depicted by the red open squares, orange open squares, black open circles, and red open circles. The color bar above (a) shows the temperature scale of the cloud top temperature.

ers the observed phase speed (c_H) for every known azimuth of the zonal (V_x) and meridional (V_y) winds which are given mathematically as:

$$c_H = V_x \cos \phi + V_y \sin \phi, \tag{4}$$

235   where ϕ is the direction of the wind ($V_H = V_x \cos \phi + V_y \sin \phi$) along the wave's propagation direction. Equation 4 is satisfied when V_H approaches c_H and the intrinsic frequency Ω approaches zero at the critical layer. This theory demonstrates the dependency of the intrinsic frequency of atmospheric waves on the background wind. The 3D blocking diagram and its projection in 2D are presented in Figure 6. The forbidden regions (regions where wave propagation is not allowed) from 0 - 17 km in the red rings correspond to the characteristics of the wind in the troposphere. The wind characteristics between the tropopause

240   and mesopause, extending from 18 - 87 km, are represented by the light blue rings, whereas above 87 to 100 km, the wind are
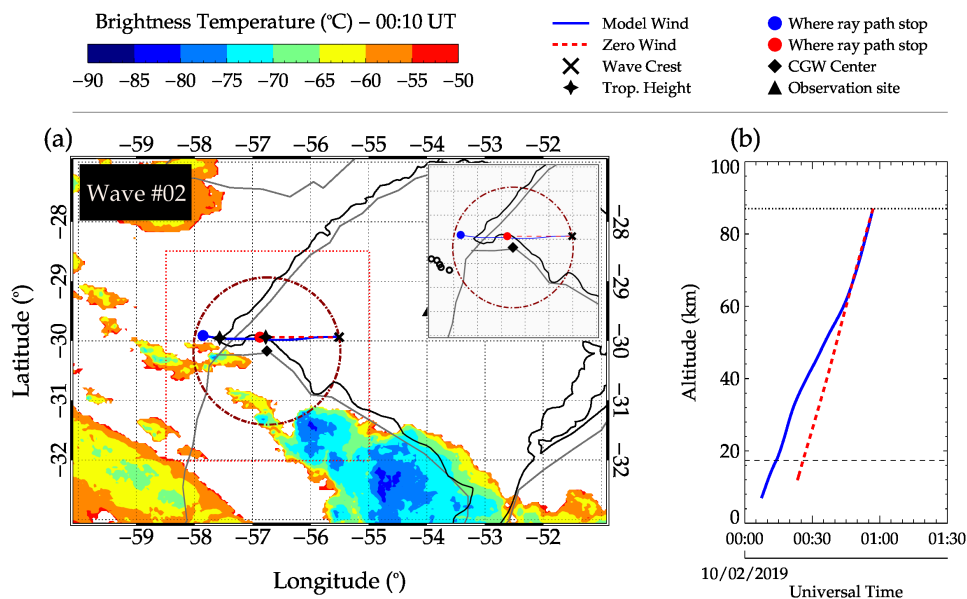
Figure 4. Ray tracing results of concentric gravity waves (CGWs) case two (#02) on October 1 - 2, 2019 with the same symbols as defined in Figure 3. The black open circle in the zoom-in region represents the only convective core (C #1).
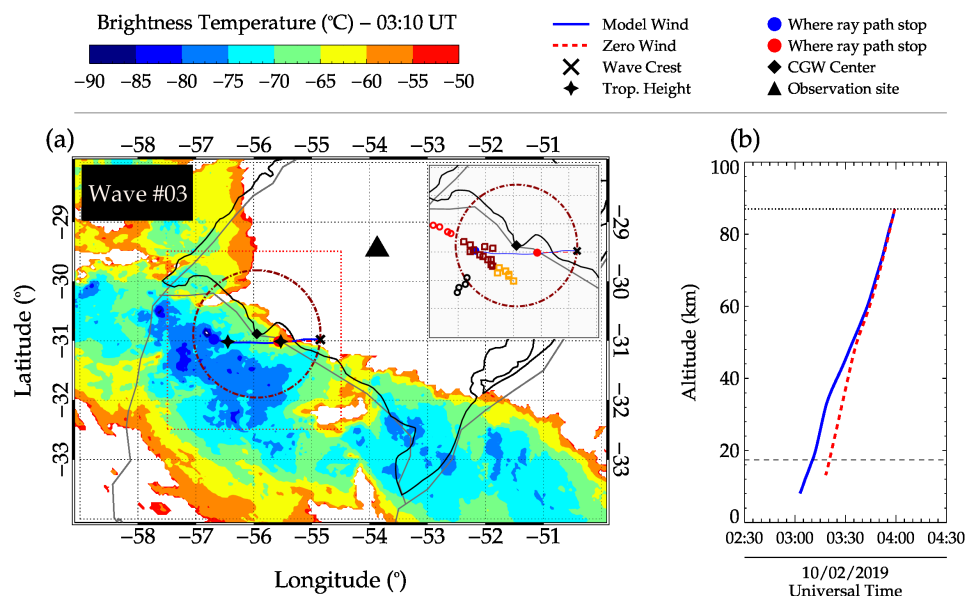
Figure 5. Ray tracing results of concentric gravity waves (CGWs) case three (#03) on October 1 - 2, 2019 with the same symbols as defined in Figure 3. The symbols in the zoom-in region have the same meaning as Figure 3.

shown by the green rings. Figure 6 was obtained using the average winds between the hours of 21:00 UT on October 1, 2019 to 05:00 UT on October 2, 2019.

From Figure 6a, weak winds were observed below the mesopause. Even though variations in the magnitude of the winds were observed, the 2D projection showed that the wind between the mesopause and the ground did not exceed 45 m/s. Note

245 that the minimum phase speed among the three CGWs is ∼73 m/s which is higher than the maximum wind in the eastward direction. The colors used in the demarcation of the winds at each respective altitude range in Figure 6a are the same in Figure 6b. Figure 6b shows that the winds in the troposphere, stratosphere, and mesosphere were mainly within the northeastern to southeastern direction. The blue arrows represent the magnitude and direction of the CGWs (on the right). The thick dashed circle is set to 30 m/s whereas, the dotted circles are in an interval of 25 m/s.
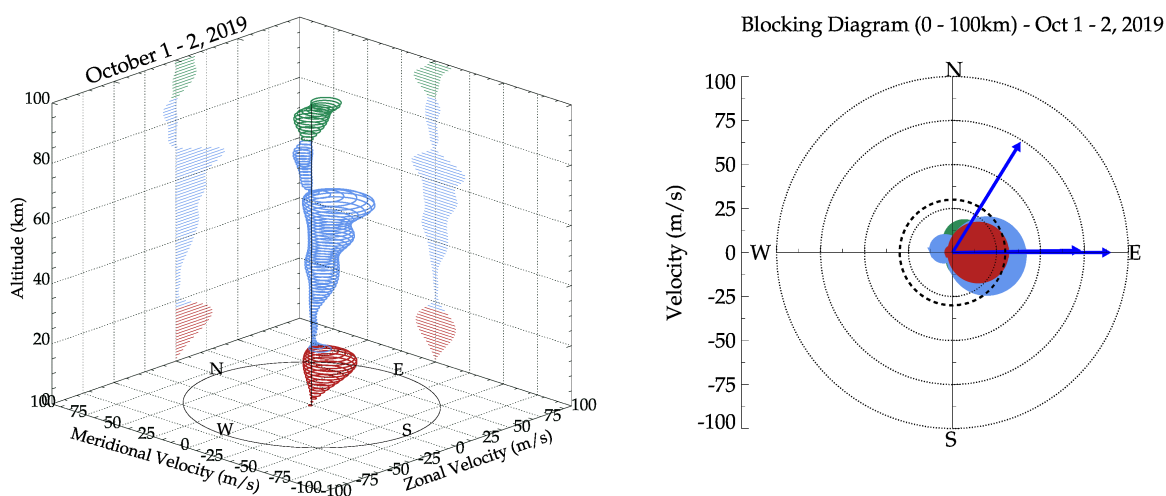
Figure 6. 3D blocking diagram for the night of October 1 - 2, 2019 in the left panel and its 2D projection in a polar plot in the right panel. For details see text.

250 The effects of the wind on wave filtering are investigated using the 3D and 2D blocking diagrams. In the 2D blocking diagram, the magnitude and direction of the horizontal phase speeds of the CGWs are the blue arrows extending from the origin. The blocking regions where wave propagation is not allowed showed quite a directional anisotropy, mainly between the north and east directions. Between the tropopause and mesopause, the winds were mostly between 31° - 109° with a magnitude < 45 m/s. This explains the propagation of the CGWs to the OH emission altitude with little or no filtering

255 without distortion of concentric shape. As depicted by the ray tracing results (Figures 3, 4, and 5), the background winds were relatively weak during the three CGWs events, and hence the small variation in the ray path of the model wind compared to that of zero winds, especially for Waves #01 and #03. It is worth mentioning that winds less than 30 m/s are considered weak (Vadas et al., 2009b) and not capable of distorting the wavefront of CGWs. For this reason, a 30 m/s threshold was set (thick dashed circle in Figure 6) to make a demarcation between weak and strong winds. However, the waves observed this night

260 have high phase speeds with respect to the average wind, therefore this criterion cannot be applicable to these cases.

3.3 Convective Sources

Convective overshooting of the tropopause by 1 - 3 km into the stratosphere can generate atmospheric gravity waves (e.g., Lane et al., 2003; Vadas et al., 2009a; Yue et al., 2009; Nyassor et al., 2021). As mentioned earlier, the CTBT from the GOES-16 IR imagery was used to identify the overshooting convective tops, which are possible sources of the observed CGWs. Numerous

265 works (e.g., Sentman et al., 2003; Vadas et al., 2009b; Yue et al., 2009; Nyassor et al., 2021) related mesospheric OH gravity waves with concentric wavefronts associated with the convective activity of thunderstorms, particularly with overshooting convective cores of these highly active cloud systems. Using the GOES infrared images, Bedka et al. (2010) used CTBT to detect overshooting tops. Yue et al. (2009), identified simultaneously regions of convective overshooting using reflectivity data from the Next Generation Weather Radar (NEXRAD), and concluded that two convective plumes were the source of the two

270 interfering CGWs studied in their work. They also noticed that the thunderstorm was already very active with strong convective activity 3 - 4 h before the CGW observations.

Around 18:40 UT a warm cloud band started to develop convective regions around 32.0°S, 55.0°W, which grew up to a large Mesoscale Convective System extending from the north-western to the south-eastern part of São Martinho da Serra, Brazil, and into the Northern part of Uruguay, was seen in the GOES-16 IR images. Just one hour later, at 19:40 UT, their cloud tops

275 reached about -65°C, showing an extremely fast vertical growth indicative of strong updrafts already in the early stages of this thunderstorm development. In half an hour, that is, at 20:10 UT, the cloud tops reached about -70°C, which is a characteristic of intense convection, the convection started to become organized into a multicell MCS. As shown in Figure 7, by 22:40 UT, we could clearly identify convective cloud cover of the main part of the system, over Uruguay, assumed circular shape, which lasted for more than 24 h. An animation of the evolution of the MCS between 18:00 UT on October 01, 2019, and 05:50 UT on

280 October 02, 2019 is provided in the video supplement.

Radiosonde measurements taken at Santa Maria (29.69°S, 53.81°W) from September 29, 2019 to October 10, 2019 at every 00:00 UT and 12:00 UT were used to obtain the tropopause height and temperature. The tropopause altitudes and temperatures for the 00:00 UT and 12:00 UT soundings at Santa Maria for each day were considered in this analysis. The results of the variations in the tropopause altitudes and temperatures are demonstrated in Figure 8. The radiosonde measurement at Santa

285 Maria on the night of the CGW events recorded a convective available potential energy (CAPE) value of ∼1500 J/kg (maximum updraft velocity of ∼54.45 m/s). During this event, hail events were reported by Globo News (2019). The hail event according to the source began at the late hours on October 1, 2019, to the early hours of October 2, 2019.

In Figure 8a, the variations in the tropopause temperature profiles are presented. The grayscale background regions of the temperature profiles labeled "T (°C)" are used to indicate the cloud top brightness temperature ranges for each day. It was

290 observed in the tropopause temperature variations that the presence of deep convection with colder cloud tops brightness temperatures further decreases the tropopause temperature Kim et al. (2018). This is the case from 12:00 UT on September 30, 2019, when the cloud top temperature ranges between -40°C to -90°C to 12:00 UT on October 3, 2019. As the deep convection dissipates and their cloud top becomes hotter, the tropopause also becomes hotter as shown in the profiles from 12:00 UT on
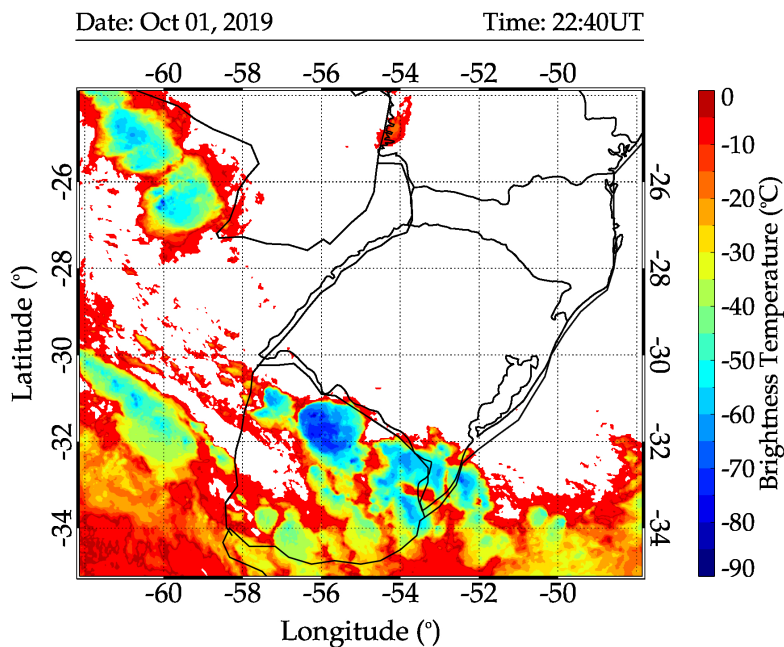
Figure 7. GOES-16 IR image taken at 22:40 UT showing the CGW generating MCS over Uruguay. This was the first image in which it was possible to identify that the main convective region of the system had assumed a clearly circular shape.

October 3, 2019, to October 10, 2019. In Figure 8b, the general behavior of the temperature from $0-23$ km is presented with
295   the variation in the tropopause altitude over-plotted in white solid lines with dots.

Since the tropopause temperature at the time of the wave event has been observed to be influenced by the presence of the active deep convection, average tropopause temperatures (of the days considered with and without deep convection) were used in the determination of the overshooting. Also, average tropopause altitude was computed. The average tropopause temperature and altitude were found to be ~-74°C and 17 km, respectively.

300   Using the two approaches of overshooting tops estimation following the techniques of Griffin et al. (2016) and São Sabbas et al. (2009) highlighted in Section 2.2, the extension by which the tropopause was overshot into the stratosphere was estimated. The result of the overshooting top variation using the method of Griffin et al. (2016) is shown in Figure 9 for each wave (i.e., Waves #01, #02, and #03) with the several overshooting convective cores (C #01,.., #04). Each wave and its corresponding overshooting convective cores in time and space are described in detail in Figures 9 and 11, respectively.

305   Figure 9 presents the temporal variations in the overshooting convective cores of each wave. For Waves #1, the dark red square, orange square, black circle, and red circle represent the convective cores (C) #1 to #4 for Wave #1 on October 1, 2019 from 21:00 to 00:00 UT on October 2. With the same symbols as Wave #1, the temporal variations in the overshooting convective core for Wave #3 between 02:00 - 04:10 are presented. For Wave #2, only convective core (C) #1 represented by the black circle was observed with overshooting between 00:30 - 01:30 UT.
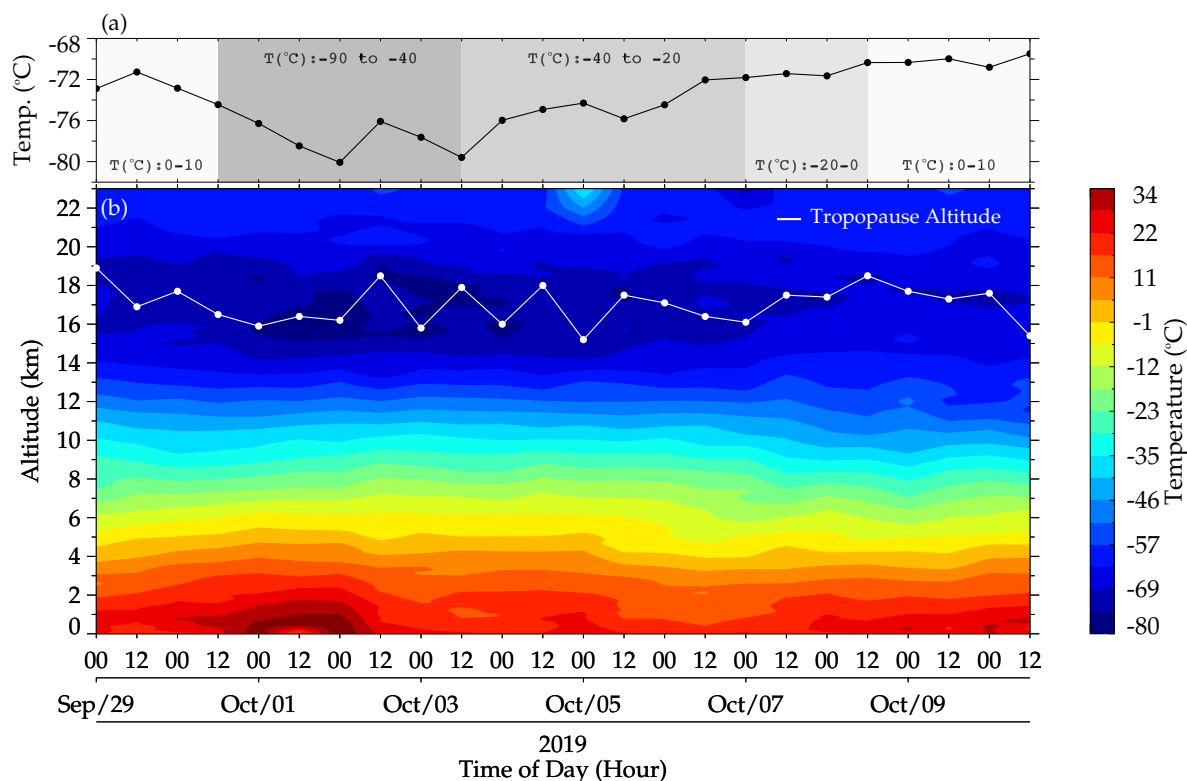
Figure 8. Tropopause temperatures and altitudes variations at Santa Maria, RS, Brazil, from September 29 to October 10, 2019, obtained from radiosonde sounding measurements at 00:00 UT and 12:00 UT. In panel (a), the variation of the tropopause temperature (black solid line with dots) along the days is presented. The grayscale regions with the label "T(°C)" represent the temperature range of the cloud top. The contour plot in panel (b) shows the temperature profile from 0 – 23 km along the days considered. The white solid line with dots shows the variation of the tropopause altitude with their respective temperatures shown in (a).

310   In Figure 11, the spatial distribution of the overshooting convective cores presented in Figure 9 is presented. Each of the symbols for Wave #1 - 3 are the same as those used in Figure 9. The other symbols: dark red dashed line, solid line, dashed-dotted circle, red dashed triangle, cross, diamond, star, and red and blue filled circles are the same as those defined in Figures 3, 4, and 5.

The ray tracing result of Wave #01 showed that the time when the ray paths of both model and zero winds reached the

315   tropopause was 23:27 UT and 23:32 UT, respectively. Four different vigorous convective cores were observed at the time the model wind ray path indicates the Wave #01 was launched. The ones that fell within the time range when the ray path reached the tropopause were C #03 and C #04 of Wave #01. It is important to note that the maximum error estimated in the propagation time for the ray path of this wave from the mesopause to tropopause considering three different ray tracing paths from three different starting positions on the first visible CGW crest, was ±24 min. These three different ray tracing starting position were
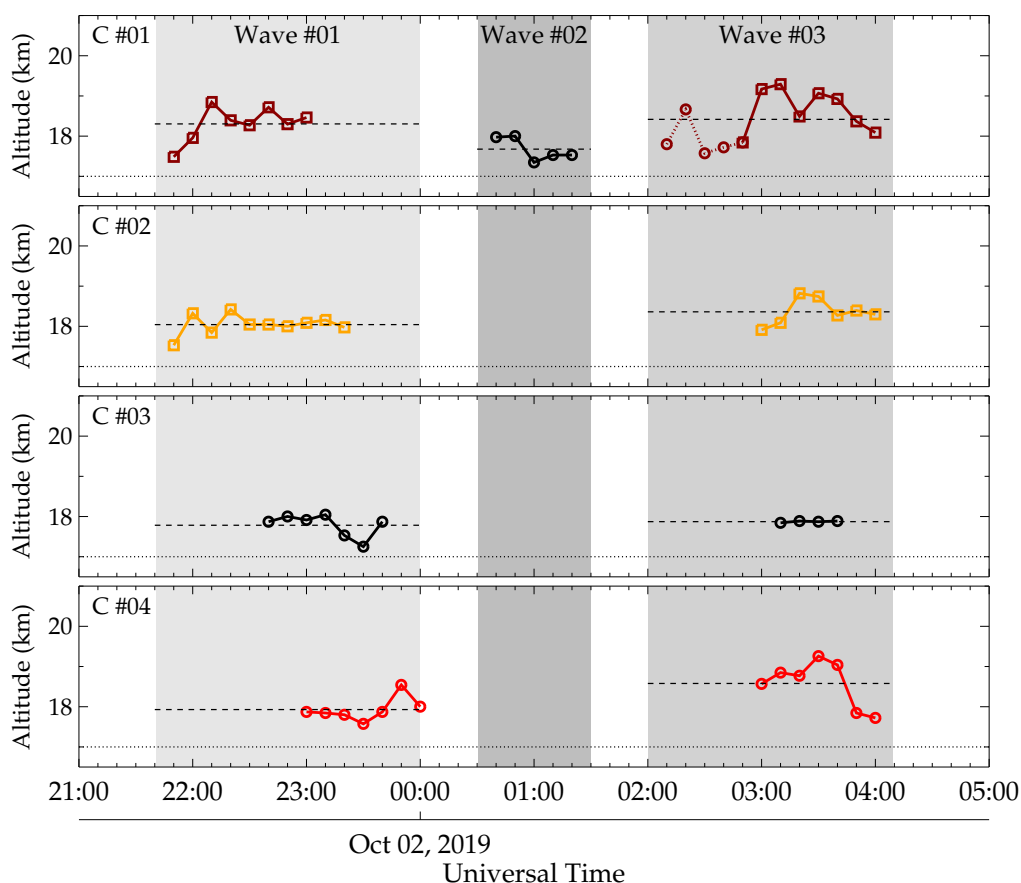
Figure 9. Tracking of overshooting in time. Subfigures (a), (b), (c), and (d) show the temporal variation of the overshooting of convective cores (C): #01, #02, #03, and #04 for the three concentric gravity waves (CGWs), Wave #01, Wave #02, and Wave #03. The greyscale regions demarcate the regions for each wave event. The dashed lines show the mean overshooting height of each system, whereas the dotted lines show the mean tropopause height between September 29 to October 10, 2019.

320   considered in order to study the influence of the wind on each ray path in several directions in order to have a general idea of the possible source locations. Taking the error into consideration, three CTBT images before and after 23:27 UT were used to track the overshooting in time, unless the core being tracked dissipates rapidly. This rapid dissipation of a core within the given time range can be seen in the case of C #03, where there was no overshooting after 23:40 UT. In such a case, the 20 min remaining in the forward tracking time was added to the reverse tracking time, setting the starting time to 22:40 UT. In Table

325   2, the details of the overshooting tops: waves, convective cores, average overshooting heights, peak overshooting heights, and the time of the overshooting are summarized. The results were obtained using the method of Griffin et al. (2016) (M #01) and São Sabbas et al. (2010) (M #02).

Table 2. Characteristics of Overshooting Tops (OTs) of the Convective Cores (C) during the October 1 – October 2, 2019 CGW Events

Wave #	Trop Height (km)	Convective Core (C)	Mean OT (km)		Peak OT (km)		Peak OT Time
			M #01	M #02	M #01	M #02	
01	17.00	#01	18.30	19.10	18.85 ± 0.39	19.98 ±0.80	22:10
		#02	18.04	18.68	18.42 ± 0.31	19.28 ± 0.50	22:20
		#03	17.78	18.26	18.05 ± 0.12	18.69 ± 0.30	23:10
		#04	17.93	18.49	18.54 ± 0.27	19.48 ± 0.50	23:50
02	17.00	#01	17.68	18.10	18.00 ± 0.17	18.61 ± 0.40	00:50
03	17.00	#01	18.42	19.28	19.29 ± 0.45	20.70 ± 1.00	03:10
		#02	18.36	19.19	18.83 ± 0.39	19.93 ± 0.70	03:20
		#03	17.87	18.40	17.88 ± 0.90	18.43 ± 0.30	03:10
		#04	18.58	19.50	19.25 ± 0.29	20.64 ± 0.90	03:30

The peak OTs of C #03 and C #04 of Wave #01 and their occurrence time fell within the error range in time when the ray path of this wave reached the tropopause. However, tracking these overshooting tops in space (shown in Figure 11), we observed that the OTs positions of C #03 and C #04 of Wave #01 were far (~50 km) from the determined center and the ray path position at the tropopause. Also, it is worth noting that Wave #01 had already reached the OH airglow layer before the observation started. Hence, the exact time when the wave first appeared in the OH image could not be obtained. This increases the difficulty in identifying the approximate source position and time using the ray tracing model.

To increase the region within which the overshooting convective cores will be considered, an average tropopause position for three different zero wind ray traced paths starting from three different positions on the first visible concentric crest was computed. Here, we consider the case of Wave #01 as shown in Figure 10.

The left panel of Figure 10 shows the map of the CTBT image at 22:30 UT (similar to Figure 3). The cross symbols depict the positions where the ray tracing began and the dashed-dotted circle shows the first visible concentric crest to appear in the OH image, respectively. Each color of the '×' corresponds to the circles of the same colors which were constructed from the tropopause diameters, and the rectangle, that was constructed from the estimated errors in longitude and latitude in the ray paths (zero and model winds). The black dashed rectangle was constructed from the extreme positions of the three rectangles. The right panel of Figure 10 is the pictorial description of how the diameter of the tropopause was estimated. The "Radius (R) = 154 km" above the horizontal line extending from the middle (the vertical dotted lines) shows the radius of the cone in 2D at the OH emission altitude. This radius is the same as the radius of the first visible concentric structure in the OH images. The vertical dotted line indicates the height of the cone. The red horizontal solid line indicates the diameter of the tropopause,
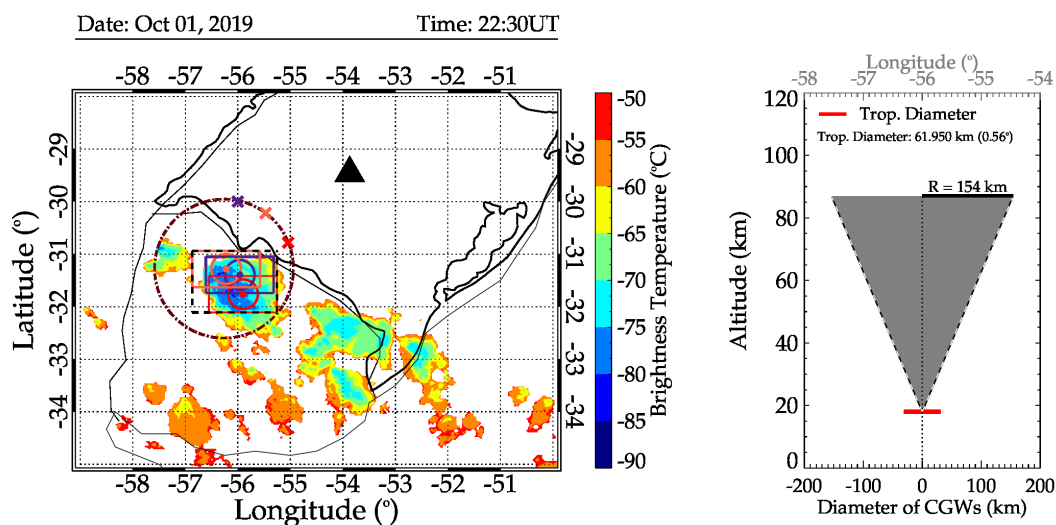
Figure 10. Description of how the region where overshooting convective cores were considered to determine the overshooting tops tracked in space and time. The black triangle, cross symbols ('×') and dashed-dotted circle are the same as defined in Figure 3. Each color of the '×' corresponds to their respective solid circles, filled circles and rectangles. The black dashed rectangle was constructed from the extreme positions of the three rectangles. In the right panel of Figure 10 is the pictorial description of how the diameter of the tropopause was estimated. The red horizontal line depicts the tropopause diameter. The black vertical dashed lines depict the height of the cone with radius (R). The vertical slanted dashed lines at either side of the black vertical dashed lines show the propagation of the CGWs after the tropopause has been overshoot.

and the black and white vertical slanted dashed lines extending vertically at either side of the dotted line are used to demarcate the propagation of the CGWs above the tropopause after the overshooting of the tropopause.

To determine the tropopause diameter, the concept of a conical propagation configuration of CGWs was used Vadas et al. (2009b); Nyassor et al. (2021). The base of the cone with a radius (same as the radius of the CGWs) of 154 km was set at an altitude of 87 km. We then followed the slant heights of the cone, thereby determining the radius at each kilometer until we reached the vertex of the cone. The vertex of the black and white dash line-slanted path is above the tropopause. The radius at the tropopause (i.e., the red horizontal line in the right panel of Figure 10) is ∼31 km (diameter of ∼62 km). Considering that a typical diameter of a convective plume is 15 - 20 km Vadas et al. (2009a, 2012) and also taking into account the dome-like protrusion shooting out of the anvil of the convective system, we set the diameter of the overshooting region to the diameter of the plume at the tropopause. It is important to determine the diameter of the plume at the tropopause in order to approximate possible regions within which overshootings are most likely to occur.

Next, we constructed rectangles around each circle constructed using the plume's diameter at the tropopause as shown in the left panel of Figure 10. Each respective rectangle was constructed by adding the error in the model wind ray path of the wave in longitude to the zonal (i.e., right and left) sides of the circles and the error in the model wind ray path of the wave in latitude

360 to the meridional (up and down) side of the circles. The estimated errors in longitude and latitude of the Wave #01 (Figure 3) are ±40 km and ±7 km, respectively. Using the extreme points of the individual rectangles for the three ray paths, the black dashed rectangle was constructed. The overshooting convective cores within the black dashed rectangle were considered for tracking the overshooting tops. A similar procedure was applied for the other two CGWs events (i.e., Wave #02 and Wave #03) to determine their respective region within which the overshooting convective cores were considered.
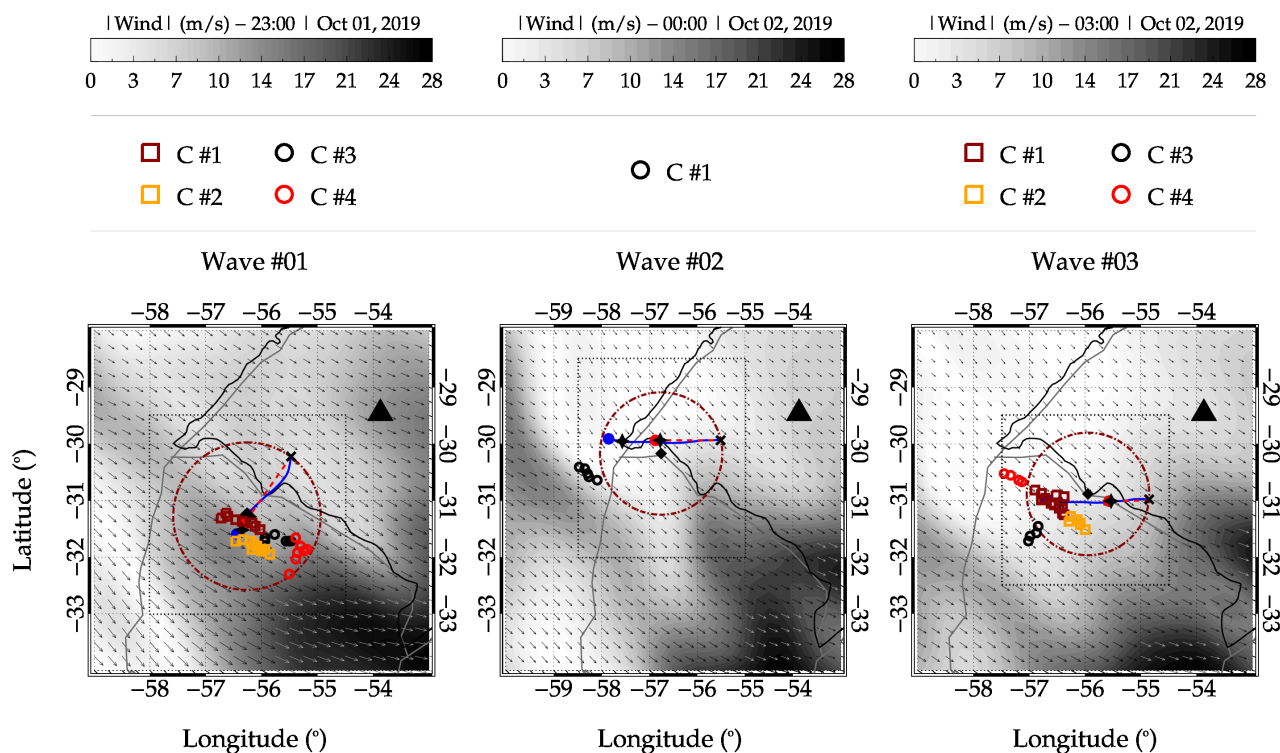
Figure 11. Tracking of overshooting in space for each concentric gravity wave (CGWs). (Left) The overshooting positions in space for Wave #01, (middle) Wave #02, and (Right) Wave #03. All symbols have the same meaning as in Figures 3, 4, and 5. Over-plotted in this figure is the vector plot of the ECMWF Reanalysis 5th Generation (ERA5) wind at the 17 km altitude, i.e., near the tropopause, at the time when the ray paths reached the tropopause. The dark red square, orange square, black circle, and red circle represent the convective cores (C) #1 to #4 for Waves #1 and #3. In the case of Wave #2, the black circle represents the convective core #1.

365   As mentioned earlier, Wave #01 had already reached the OH emission altitude before the observation began. Also, the observed overshooting convective cores in the cloud top brightness temperature image at the time when the ray paths reached the tropopause, were quite far. For the black circles (C #03), no significant variations were seen in the OTs until between 23:10 UT and 23:40 UT. Similarly, the red circles (C #04) showed a variation between 23:30 UT and 23:50 UT. Even though these two cores (C #03 and C #04) overshot more than 1 km (see Figure 11 and Table 2) and not knowing the exact time the

370 wave first appeared on the image, these OTs could possibly not be the source of Wave #01. Also, the time of the peak OT

altitude of C #04 occurred after the estimated time when the ray paths of Wave #01 reached the tropopause. Even if the wave first appear in the OH images at 00:27 UT, this further strengthens the fact that C #04 (black circle) cannot be the source of Wave #01. Note that, the spatial distribution of C #04 is quite far from the identified source location.

375   Still considering the existence of Wave #01 in the OH emission layer before the observation began, we tracked the OT back further in time to see if there were overshootings of the tropopause. Two other convective cores: (a) C #01 and (b) C #02 were observed with higher OTs within the hours of 21:50 UT and 23:00 UT, and 21:50 UT and 23:20 UT, respectively. C #01 had large OT variations during the entire time the core was active with a peak OT altitude of 18.85 km at 22:10 UT. Variations were also observed in the profile of C #02, especially within the hours of 21:50 UT and 22:30 UT with a peak OT altitude at 18.42 km at 22:20 UT. Tracking Cs #01 and #02 in space, we observed that the distributions (the dark red and orange squares) of these

380   two OTs were closer to the source locations of Wave #01 especially C #01. Considering the variations observed in the OTs (C #01 and C #02 in Figure 9), their peak OT altitudes, time of peak OT, and their distributions in space around the identified source locations showed these two convective cores are the most likely cores that overshot to excite Wave #01. Note that there were no other active convective cores seen within the error ranges in longitude and latitude considered beyond 21:50 UT.

We now examine the details of the convective cores (C) of Wave #03. Similar to Wave #01, four convective cores; C #01,

385   C #02, C #03, and C #04 were tracked in space and time. For C #01, C #02, and C #04, variations in the OT altitudes were observed (see Figure 9). The peak OT altitudes of C #01, C #02, and C #04 occurred at 19.29, 18.83, and 19.25 km and 03:10, 03:20, and 03:30 UT, respectively. Interestingly, the ray tracing results showed that the ray paths of zero and model winds reached the tropopause at 03:10 and 03:20 UT (the estimated excitation times). These estimated times agreed with the times the highest OT altitudes were observed in Figure 9 for C #01 and C #02 of Wave #03. The spatial distributions of C #01 and C

390   #02 (dark red and orange squares) in the right panel of Figure 11 revealed the OT locations were close to the identified source locations by ray tracing and the determined center especially for C #01.

Even though the time of peak OT altitude of C #04 (red circles) was within the error range, the spatial distribution of this core was found outside: (a) the first visible concentric crest and (b) the error range in longitude and latitude. Therefore, C #04 has a lesser probability of being the source of Wave #03. Also, C #03 (black) was found to be outside the error range in

395   longitude and latitude. The temporal variation in the OT altitudes of C #03 had a peak altitude of 17.88 km at 03:20 UT. The peak altitude of C #03 and C #02 occurred at the same time. However, with C #02 having ∼0.93 km OT altitude higher than C #03 and also closer to the source location, C #03 cannot be the overshooting that generated Wave #03.

Wave #02, on the other hand first appeared on the OH airglow images at 00:55 UT and disappeared around 01:07 UT. However, the backward ray tracing result showed that the ray path of this wave reached the tropopause at around 00:15 UT and

400   ∼140 km away from the nearest overshooting convective core. Also, the determined center was ∼220 km away. From Table 2, C #01 of Wave #02 occurred at 00:50 UT with a peak OT altitude of 18.00 km. Further analysis on the time of the peak OT altitude showed that this overshooting cannot be responsible for the generation of Wave #02 if the wave was first visible at 00:55 UT in the OH images and the highest overshooting occurred at 00:50 UT. This wave could not propagate to the OH emission layer within 5 min considering the temporal scale of the wave. Since the identified source was not overshooting at

405   the time the ray path reached the tropopause and also not having active convective cores ±30 min within the error range in

longitude and latitude, this wave could be excited by other mechanism and since this is out of scope of the current work, this wave will be left for further investigation in future work.

It is important to mention that the tracking approach used by São Sabbas et al. (2009) was employed to identify the most likely convective core that overshot to generate these three CGWs. This method was used because the MCS during this night was moving southeastward at an average speed of ~0.1°/10 min (11 km / 10 min). Also, as shown by the vector plot (the gray arrows) in Figure 11, the wind at the tropopause was towards the southeastern direction throughout the entire period of the wave events. Also in Figure 11, the magnitude of the winds at the tropopause is presented in the grey contour with the color bars showing their respective scales.

As mentioned earlier, two methods were used to estimate the overshooting tops: (i) Griffin et al. (2016) (M #01) and (ii) São Sabbas et al. (2010) (M #02). A comparison between the two methods showed that the OT altitudes estimated using the method of São Sabbas et al. (2010) agrees well with Griffin et al. (2016), since the error bars overlap each other (Figure 12). The error in both methods was estimated by calculating the propagation error of each measurement. To estimate the propagation error, the standard deviation of each variable is computed and multiplied by the derivative of the variable. The product of the variables and its derivatives are summed over the data set to obtain the propagation error. This procedure follow the propagation error analysis presented by Bevington and Robinson (2003). As shown in Figure 12, the maximum estimated errors are ~±0.6 km for the method of Griffin et al. (2016) (M #01) and ~±0.9 km for the method of São Sabbas et al. (2010) (M #02).

3.4 Other Severe Weather Associated Events

Other severe weather-associated events such as intense lightning activities, hail, and Transient Luminous Events (TLEs) were observed during the period of these CGWs events. The lightning activities were recorded by the Brazilian Lightning Detection Network (BrasilDAT) sensors. Using the same technique employed in Nyassor et al. (2021), the locations with the highest lightning densities were found to coincide with the location of the coldest cloud tops (overshooting tops) as shown in Figure 13. The lightning densities were obtained by binning the positions of the lightning strike into 0.06°×0.06° (6.6 km× 6.6 km) grid boxes.

Comparison between the spatial distribution of the lightning strikes and the MCS clearly showed a direct relationship between the two phenomena. Several studies, for instance, Medeiros et al. (2003), Wrasse et al. (2003), Xu et al. (2015) and Nyassor et al. (2021) showed relationship between GWs/CGWs and deep convection. Xu et al. (2015) observed strong lightning activities within the summer season where quite a lot of CGWs were observed.

In a CGWs study, Yue et al. (2013) observed lightning flashes around the center of the Typhoon-generated CGWs. The point-like source of convective CGWs, that is, overshooting of the tropopause as mentioned earlier, have been related to strong updraft activities within deep convection. Nyassor et al. (2021) and references therein showed the direct relationship between intensity/density of lightning activities in space and overshooting tops of deep convection by the strong updraft. Nyassor et al. (2021) further found that regions with a high density of lightning spatial distribution agree with the coldest regions of the CTBT. Previous studies of Bedka et al. (2010) demonstrated that CTBT with a temperature greater than 200 K or less than
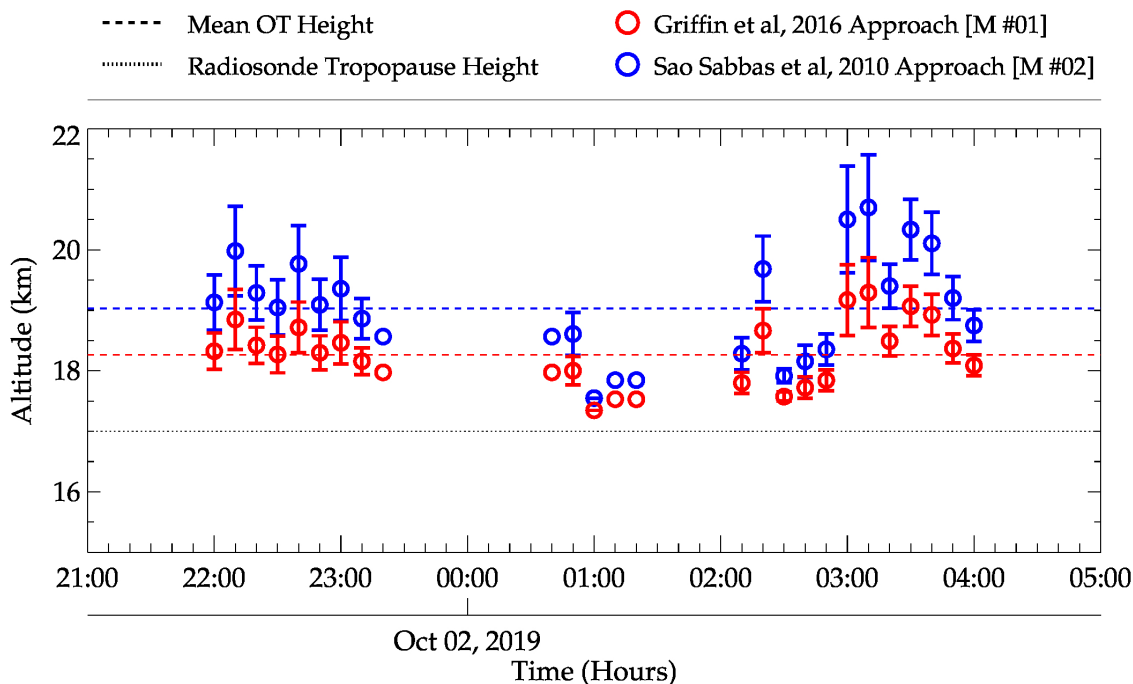
Figure 12. Comparison between the two OT altitude estimation methods. The comparison between the OT altitudes, red open circle with the error bar for the Griffin et al. (2016) method, and open blue circle with the error bars for the São Sabbas et al. (2010) method. The radiosonde tropopause height is depicted by the black dotted lines and the mean OT height shown by the dashed lines; red for Griffin et al. (2016) and blue for São Sabbas et al. (2010).

-73.15°C have a higher occurrence of lightning activities within 10 km around the overshooting tops. In Figure 13, it was observed that the lightning activities have high densities in regions where the CTBTs are very cold. This signifies overshooting tops.

Several Transient Luminous Events (TLEs), especially sprites, were also observed during these CGWs events. Here we report the occurrence of two sprite events registered with the LEONA TLE station installed at the Southern Space Observatory (SSO). The first event occurred at 00:42:28 UT and the second occurred at 00:46:51 UT of October 2, 2019. Both events are shown in Figure 14.

Sprites are short duration plasma discharges and low intensity optical emission observed at night. They are generated by the quasi-electrostatic field established by charge extinction within the thunderstorm resulting from lightning discharges, predominantly of positive Cloud-to-Ground (+CG) lighting. In the upper atmosphere above cloud tops (at ∼12 - 20 km altitude) this field extends all the way to the base of the nighttime ionosphere, at ∼100 km altitude, where it is strongly shielded by the ionospheric plasma. When a lightning discharge extinguishes enough charge inside the thunderstorm, free electrons present in the atmosphere between the cloud tops and the ionosphere can be accelerated by its quasi-static field and gain enough energy
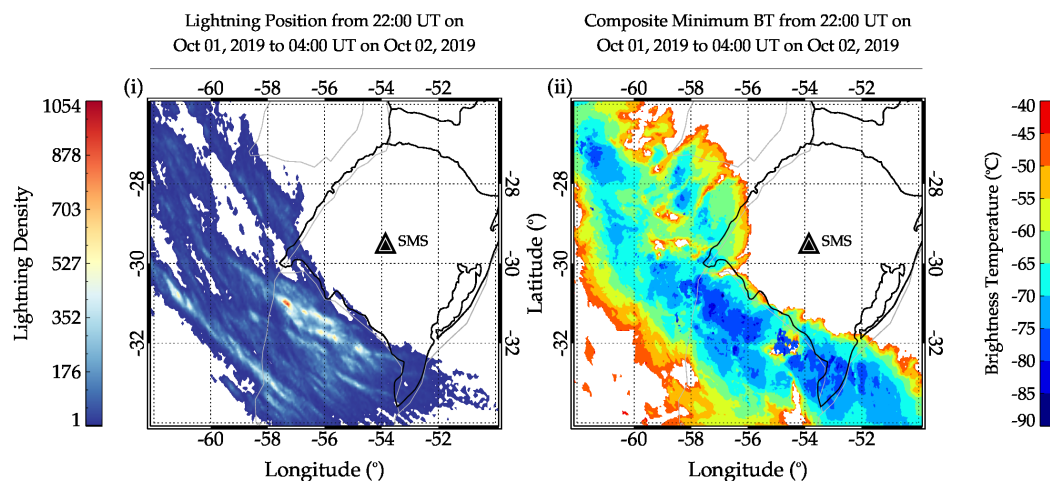
Figure 13. Comparison between the spatial distribution of lightning density and composite GOES-16 IR cloud top brightness temperature images from 22:00 UT on October 1, 2019, to 04:00 UT on October 2, 2019. The black filled triangle with white triangle shows the position of the southern space observation site.
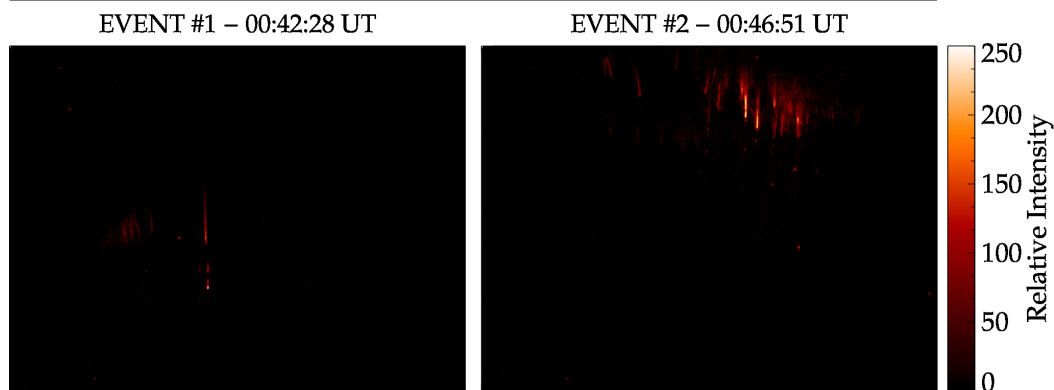
Figure 14. Image of two groups of sprites generated by the same thunderstorm that generated the CGWs observed during the night of October 1 to October 2, 2019.

to start an electron avalanche process at ~70 - 85 km altitude, which may initiate one or several plasma streamers that may form a sprite or a group of sprites. Sprites, thus initiate at ~70 - 85 km altitude and their streamers can extend down to as low as ~30 km and up to ~100 km at the base of the nighttime ionosphere (São Sabbas et al., 2010), therefore sprites pierce right through the airglow layer, at ~87 km altitude. Their lateral dimensions can be of a few tens of meters in the case of column sprites, up to ~40 km in the case of carrot sprites (São Sabbas et al., 2010, and references therein).

Both sprite events reported here are groups of column sprites, with really thin columns, possibly a few tenths of meters thick. The first event displayed one well-defined long column with two dark bands and an intense bead at the bottom, plus several
460   very faint diffuse columns on its left side. The second event was composed of at least 10 short columns, two of them very bright and the rest diffuse, all showing a broader diffuse region on the top, called hair, which is typical of carrot sprites and not very common on column sprites. This report is the first observation of sprites and gravity waves in South America.

    Sprites and CGWs have been simultaneously observed once before, by Sentman et al. (2003), in the central region of United States during a field campaign in 1999. Using low-light intensified CCD cameras, Sentman et al. (2003) observed at least
465   12 bright sprites above a Mesoscale Convective System over the state of Nebraska for a period of 2 h during which they also observed concentric gravity waves generated by the same MCS using a 25 s exposure CCD fitted with a red filter. They estimated the wave period and wavelength to be $\sim$10 min and $\sim$50 km, respectively, during the first hour of observation and $\sim$11 min and $\sim$40 km, respectively, during the second hour. They used the well-established optical intensity of $\sim$1 kR for the observed OH Meinel emission and compared it to the intensities of the sprite observed in order to estimate an upper limit
470   to the thermal energy deposited by sprites in the mesosphere, arriving to the value of $\sim$1 GJ. Since a detailed TLE analysis and comparison with the gravity wave observations is not the focus of the current study, future work will further explore the combined observations of these phenomena.

3.5   Comparison between Observed Horizontal Wavelengths and that of Dispersion Relation

To study and compare the gravity wave activity in the lower/middle stratosphere with the wave activity in the mesopause
475   region, the spectrum of the excited waves by the MCS above the tropopause and lower stratosphere was computed. To achieve this, the horizontal and vertical wavelengths, and periods were used.

    Temperature profiles from radio occultation (each sounding position shown by the white squares in Figure 15) during these CGW events were also used to study the convective system impact on the tropopause as a way to independently verify the results obtained from the radiosonde shown in Figure 8. Similar oscillations of the tropopause temperature and height were
480   identified (see Figure A1), confirming our initial results. Since the occultation profiles extend to an altitude of 50 km, the vertical wavelength spectra above the tropopause to 50 km was computed.

    Using the vertical wavelength spectra obtained from the radio occultation and the observed wave period, horizontal wavelength spectra above the tropopause and lower stratosphere was estimated using the dispersion relation of (Gossard and Hooke, 1975):

485   $$k_H = \left[\left(m^2 + \frac{1}{4H^2} \right) \omega_{Ir}^2 \times \left(N^2 - \omega_{Ir}^2 \right)^{-1} \right]^{1/2} \tag{5}$$

where m^2 is the vertical wavenumber, H is the density scale height, N^2 is the buoyancy frequency and ω_{Ir}^2 is the intrinsic frequency. The horizontal wavenumber (k_H) and observed frequency (ω_{obs}) were obtained from the CGW parameters (horizontal

wavelength [$\lambda_H = 2\pi/k_H$] and period [$\tau_{obs} = 2\pi/\omega_{obs}$]). The intrinsic frequency of the observed wave was estimated using Equation 6 (Nyassor et al., 2018);

490 $$\omega_{Ir} = \omega_{obs} - U_H.k_H \tag{6}$$

where, U_H is the magnitude of the horizontal wind in the propagation direction of the wave and the k_H is the horizontal wavenumber. The $U_H.k_H$ gives the estimate of the background wind frequency. We estimated the horizontal wavelength spectra using as input parameters in Equation 5: (a) the vertical wavenumbers at each altitude, obtained from the radio occultation using wavelet transform, (b) the intrinsic frequency of the waves, and (c) the horizontal wind obtained from ERA5 reanalysis data.
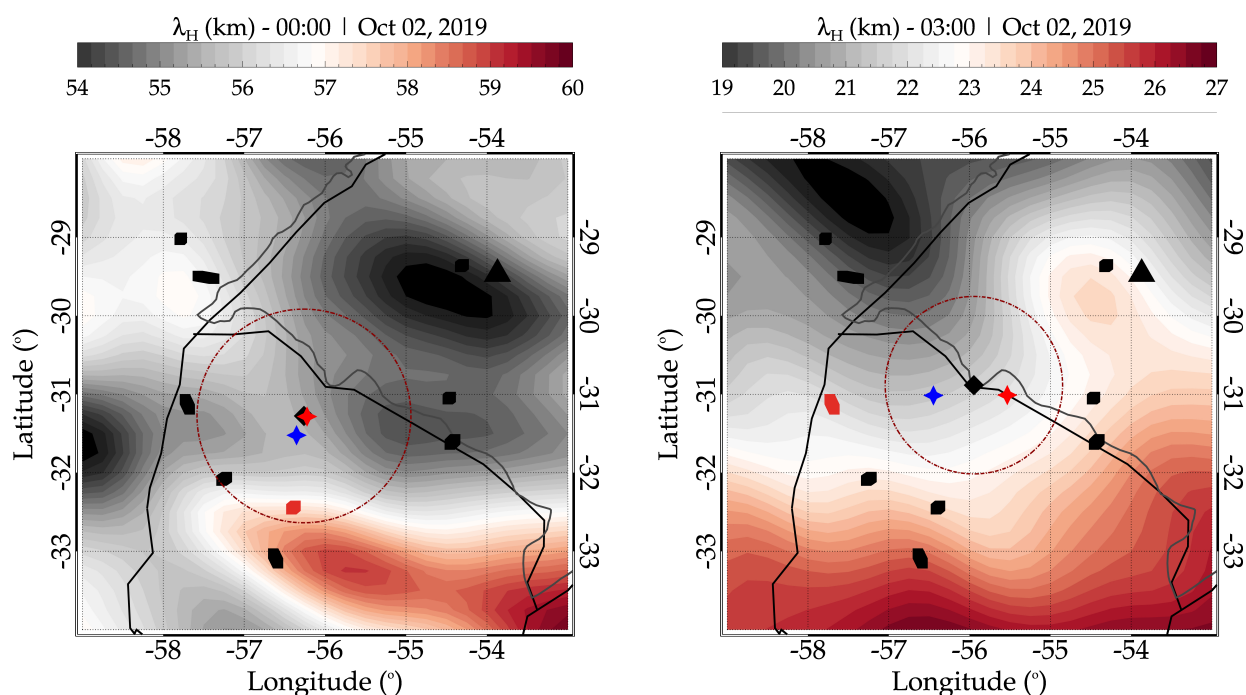
Figure 15. Horizontal wavelength spectra obtained using dispersion relation. In the left panel is the horizontal wavelength spectra above the tropopause between 00:00 and 01:00 UT whereas, between 03:00 and 04:00 UT is shown in the right panel.

495   Figure 15 shows the result of the horizontal wavelength spectra obtained using Equation 5 above the tropopause (i.e., 24 km) within a similar spatial range considered in Figure 11 for Waves #01 and #03. In the left panel of Figure 15 is the horizontal wavelength spectra above the tropopause for 00:00 - 01:00 UT whereas, that of 03:00 - 04:00 UT is shown in the right panel. The black triangle depicts the observatory location and the horizontal wavelength scale is indicated by the color bar. The black squares show the positions of the radio occultation soundings whereas, the red squares show the closest soundings to the source

500   used to estimate the vertical wavelength. Comparison between the vertical wavelengths estimated from the radio occultation temperature profiles and ray tracing showed an average value of $\sim$25 km between the altitudes of 20 and 60 km. A similar

region to Figure 11 was considered since Waves #01, and #03 were observed within the same region. The black diamond and red dotted-dashed circle have the same meaning as defined in Figures 3a, 4a, 5a, and 11. The blue and red stars (black stars in Figures 3a, 4a, 5a, and 11) represent the tropopause positions of the model and zero winds ray paths.

505   We found that the horizontal wavelength spectra above the tropopause is in agreement with the observed CGWs horizontal wavelengths. Figure 15 is used to compare the horizontal wavelength spectra radiated by the system with the observed CGWs horizontal wavelengths and also to predict the expected horizontal wavelength spectral in the OH emission altitude.

4   Summary and Conclusion

Three concentric gravity waves (CGWs) events excited by a Mesoscale Convective System on the night of October 1 to October
510   2, 2019 were studied. The three events occurred between 22:00 UT on October 1, 2019, and 04:00 UT on October 2, 2019. All three waves have partial concentric wavefronts.

Backward ray tracing results showed weak background wind. The identified sources (OTs) by the ray tracing for Wave #01 and #03 showed high overshooting tops within the spatial and temporal ranges determined using the ray tracing maximum error margin. However, the exact time when Wave #01 appeared in the OH images was not known since the wave was present in
515   OH images before the observation began. Further analysis on the source of Wave #01 by tracking the OTs further back in time within the same error ranges considered in space showed that Wave #01 was most likely excited around 22:20 - 22:40 UT on October 1, 2019, by either C #01 or #02. This is because C #01 and #02 were closer to the expected source location estimated by the ray tracing and the determined center. The identified source of Wave #02, on the other hand did not coincide with any convective core with significant overshooting. The peak OTs altitude of C #01 of Wave #02 occurred 5 min before the wave was
520   first seen in the OH image. Considering the parameters of Wave #02, this wave could not have propagated to the OH altitude within 5 min; hence it is highly unlikely that C #01 was the likely source of Wave #02.

The estimation of the tropopause height was not straightforward for the days analyzed in this work, the tropopause was colder than what is usually observed and reported in the literature. This colder tropopause could be a consequence of cooling of the upper troposphere due to the presence of this intense MCS or a consequence of the presence of Rosby waves or quasi-horizontal
525   flow, or some other large scale upper tropospheric process driven by extra-tropical dynamics. Therefore, the strategy that we adopted differed from the approach used by (Nyassor et al., 2021, and references therein). We average the vertical temperature profiles of 12 days, including days with and without convection and starting 2 days prior to the day of the CGW events. From that we established an average tropopause for those days that we used as a reference to estimate important parameters for this work, such as the overshooting vertical extent of the convective cores identified as possible sources of the observed CGWs.
530   Since these convective cores were moving together with the whole MCS, approximately 0.1° every 10 min, in order to identify the most likely sources, the convective cores with OTs were tracked in space and time. Radio occultation temperature profiles from 9 locations underneath the general area where the gravity waves were generated and observed, were analyzed to complement the radiosonde measurements when estimating the tropopause temperature and height, as well as the vertical wavelength of the radiated waves above the tropopause and in the stratosphere. From this vertical wavelength and the intrinsic

wave period, the dispersion relation of gravity waves was then used to estimate the possible horizontal wavelength spectra excited by the source. The horizontal wavelength spectra obtained from the dispersion relation compared well with that of the observed waves.

It is therefore important to mention that this work presents a new approach to investigating the approximate overshooting convective cores within deep convections located by backward ray tracing to be the possible source of observed CGWs or GWs in general.

Data availability. The data used to produce the results of this manuscript were obtained from the Southern Space Observatory at São Martinho da Serra, which is supported by the Southern Space Coordination and National Institute for Space Research. If someone would like to access these data, please contact either José Valentin Bageston (jose.bageston@inpe.br) or Cristiano Max Wrasse (cristiano.wrasse@inpe.br) or access the data online in the portal of the "Estudo e Monitoramento Brasileiro do Clima Espacial" (EMBRACE/INPE) at "http://www.inpe.br/climaespacial/portal/en"

Video supplement. An animation of the MCS during the 3 CGW events between 18:00 UT on October 1, 2019 and 05:50 UT on October 2, 2019 is provided (https://doi.org/10.5446/56980, Nyassor and Wrasse, 2022).

Appendix A: Radio occultation temperature profiles from October 1 to October 3, 2019

For verification, here we include the plot of the radio occultation profiles that verify the variations in the tropopause height and temperature observed in the radiosonde observation (Figure 8 in the main text). For the plots shown in Figure A1, only profiles taken between October 1 and 3 are presented. The profiles on the other days considered in the radiosonde profile were not available for the radio occultation profiles.

To produce Figure A1, the closest profiles within a radius of ∼400 km centered around the center of each CGWs are selected. The profiles closest to the centers of CGWs were chosen because this profile will be used to investigate the vertical wavelengths of the CGWs. For each of the days used in this plot, only three sounding profiles were found within this set region. In the upper panel is the individual profiles of the temperature between the altitude range of 0 to 60 km. The color bars define the temperature scale of the profiles. In the lower panel, the tropopause temperature for each profile is plotted as a function of altitude. From the individual tropopause temperature of each profile, the variations in the tropopause temperature along the days considered were investigated. Between October 1, 2019 and the early hours of October 2, 2019, the tropopause was within a similar range as that of the radiosonde temperature profile. Also, similar to the radiosonde profile, the tropopause temperature began to increase after the earlier hours on October 2.
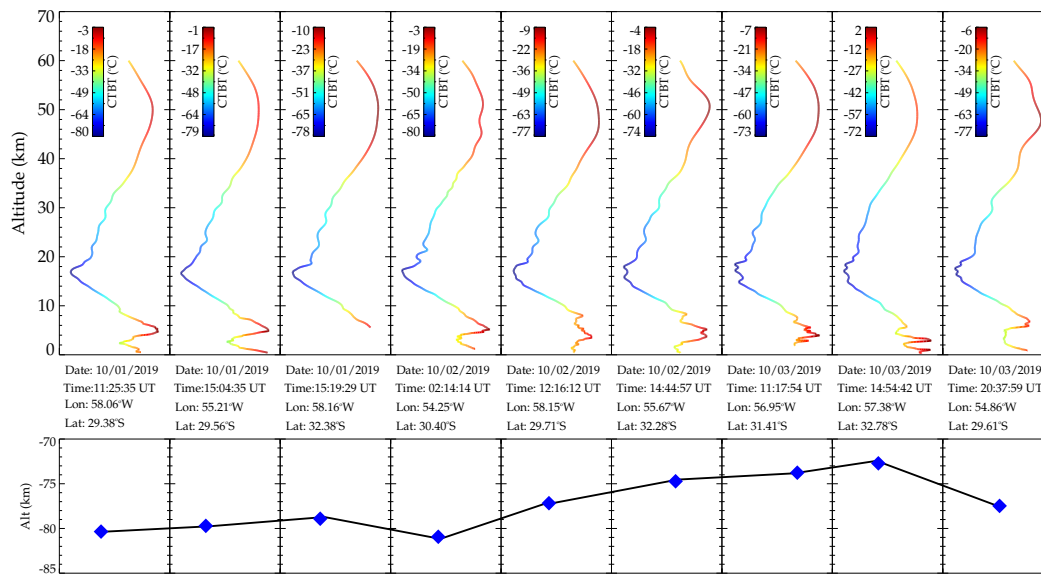
Figure A1. Radio occultation sounding profiles around the SMS between October 1 to October 3, 2019, before, during and after the October 2 CGW event.

Appendix B: Larger view of MCS around São Martinho da Serra with respect to the observed CGW
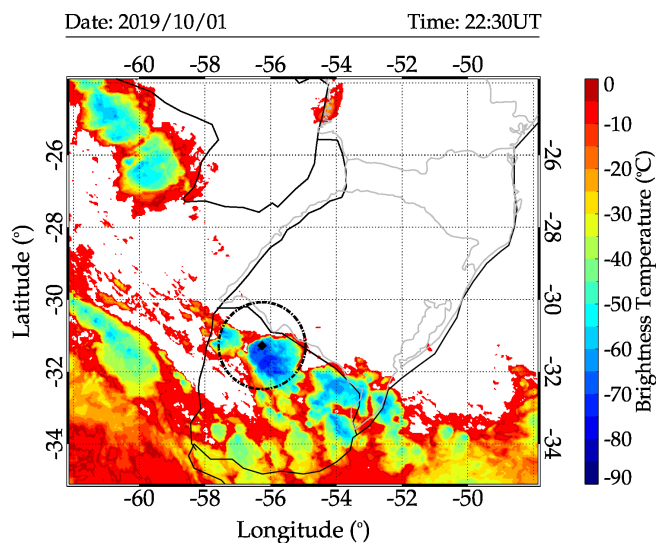
Figure B1. Same as Figure 3a in the main article but an extended coverage with the cloud top brightness temperature ranging from 0 to -90°C
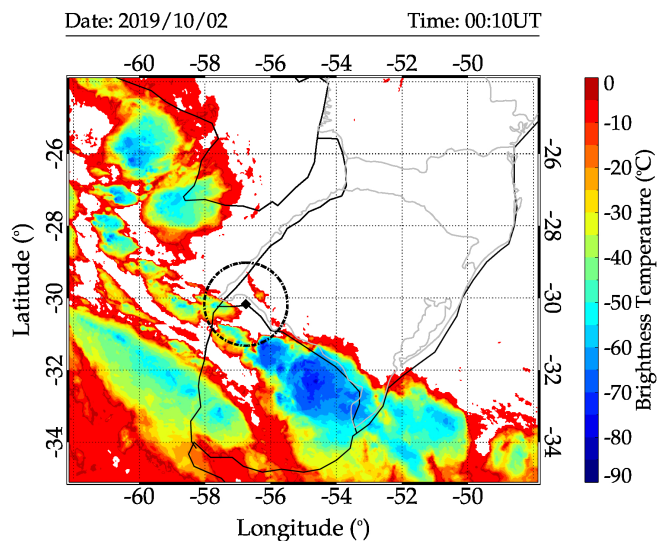
Figure B2. Same as Figure 4a in the main article but an extended coverage with the cloud top brightness temperature ranging from 0 to -90°C
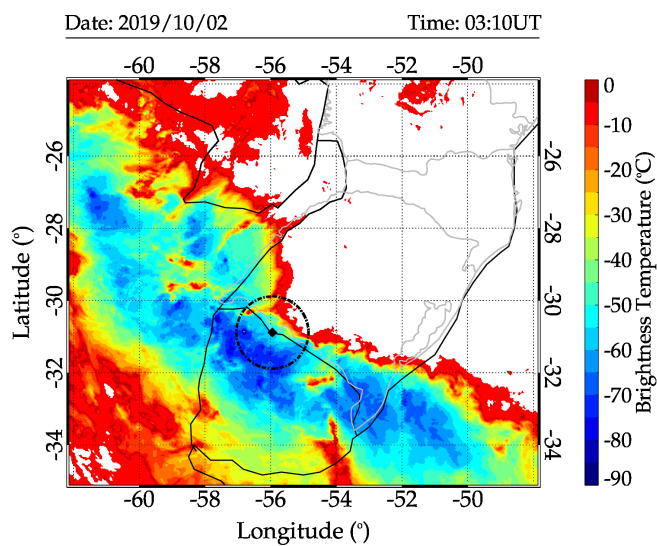
Figure B3. Same as Figure 5a in the main article but an extended coverage with the cloud top brightness temperature ranging from 0 to -90°C

Author contributions. P. K. Nyassor wrote the article and performed most of the analysis. C. M. Wrasse and I. Paulino assisted in the development and validation of the methodologies and also in the revision of the manuscript. E. F. M. T. São Sabbas helped in the development
565 and validation of the methodology used to track the convective cores in space and time. J. V. Bageaton provided the all-sky images. K. P. Naccarato provided lightning data and revised the manuscript. D. Gobbi revised the manuscript. C. A. O. B. Figueiredo assisted in the development and validation of some of the methodologies and the revision of the manuscript. T. T. Ayorinde worked on the radio occultation data. H. Takahashi revised the manuscript. and D. Barros helped in the development and validation of some of the methodologies and the revision of the manuscript.

570 *Competing interests.* The authors declare that they have no conflict of interest.

Acknowledgements. This work has been supported by the Coordenação de Aperfeiçoamento de Pessoal de Nível Superior (CAPES) and the Conselho Nacional de Desenvolvimento Científico e Tecnológico (CNPq). C. M. Wrasse, I. Paulino, H. Takahashi, and D. Barros thank CNPq for the financial support under the contract numbers 314972/2020-0, 306063/2020-4, 310927/2020-0 and 300974/2020-5. C.A.O.B. Figueiredo thanks the Fundação de Amparo à Pesquisa do Estado de São Paulo (FAPESP) support under the process numbers 2018/09066-8
575 and 2019/22548-4. E. F. M. T. São Sabbas thanks FAPESP for the grant 2012/20366-7 that enabled the creation of Transient Luminous Event and Thunderstorm High Energy Emission Collaborative Network (LEONA). The cloud top brightness temperature maps were provided by the Center for Weather Forecasting and Climate Studies (CPTEC/INPE). The lightning data were provided by the Brazilian lightning detection network (BrasilDAT) from the Earth Sciences Department (DIIAV/CGCT/INPE) supported by EarthNetworks. The radiosonde data were provided by the University of Wyoming. The Airglow images from São Martinho da Serra can be accessed online in the portal of the "Estudo e
580 Monitoramento Brasileiro do Clima Espacial" (EMBRACE/INPE) at "http://www.inpe.br/climaespacial/portal/en". The GOES-16 IR images were provided by the Center for Weather Forecasting and Climate Studies CPTEC/INPE) at "http://satelite.cptec.inpe.br/acervo/goes16.formulario.logic". The radiosonde data were obtained from the University of Wyoming through the link "http://weather.uwyo.edu/upperair/sounding.html". The lightning data were provided by the Brazilian lightning detection network (BrasilDat). The sprite data were provided by the LEONA Network.

References

Adler, R. F. and Fenn, D. D.: Thunderstorm intensity as determined from satellite data, Journal of Applied Meteorology and Climatology, 18, 502–517, https://doi.org/https://doi.org/10.1175/1520-0450(1979)018<0502:TIADFS>2.0.CO;2, 1979.

Azeem, I., Yue, J., Hoffmann, L., Miller, S. D., Straka, W. C., and Crowley, G.: Multisensor profiling of a concentric gravity wave event propagating from the troposphere to the ionosphere, Geophysical research letters, 42, 7874–7880, https://doi.org/10.1002/2015GL065903, 2015.

Bageston, J., Wrasse, C. M., Gobbi, D., Takahashi, H., and Souza, P.: Observation of mesospheric gravity waves at Comandante Ferraz Antarctica Station (62 S), in: Annales Geophysicae, vol. 27, pp. 2593–2598, Copernicus GmbH, https://doi.org/10.5194/angeo-27-2593-2009, 2009.

Bedka, K., Brunner, J., Dworak, R., Feltz, W., Otkin, J., and Greenwald, T.: Objective satellite-based detection of overshooting tops using infrared window channel brightness temperature gradients, Journal of applied meteorology and climatology, 49, 181–202, https://doi.org/10.1175/2009JAMC2286.1, 2010.

Bevington, P. R. and Robinson, D. K.: Data reduction and error analysis for the physical sciences; 3rd ed., McGraw-Hill, New York, NY, https://cds.cern.ch/record/1305448, 2003.

Boccippio, D. J., Williams, E. R., Heckman, S. J., Lyons, W. A., Baker, I. T., and Boldi, R.: Sprites, ELF transients, and positive ground strokes, Science, 269, 1088–1091, https://doi.org/10.1126/science.269.5227.1088, 1995.

Drob, D. P., Emmert, J. T., Meriwether, J. W., Makela, J. J., Doornbos, E., Conde, M., Hernandez, G., Noto, J., Zawdie, K. A., McDonald, S. E., et al.: An update to the Horizontal Wind Model (HWM): The quiet time thermosphere, Earth and Space Science, 2, 301–319, https://doi.org/10.1002/2014EA000089, 2015.

Figueiredo, C., Takahashi, H., Wrasse, C., Otsuka, Y., Shiokawa, K., and Barros, D.: Investigation of nighttime MSTIDS observed by optical thermosphere imagers at low latitudes: Morphology, propagation direction, and wind filtering, Journal of Geophysical Research: Space Physics, 123, 7843–7857, https://doi.org/https://doi.org/10.1029/2018JA02543, 2018.

Fritts, D. C. and Alexander, M. J.: Gravity wave dynamics and effects in the middle atmosphere, Reviews of geophysics, 41, https://doi.org/10.1029/2001RG000106, 2003.

Garcia, F., Taylor, M. J., and Kelley, M.: Two-dimensional spectral analysis of mesospheric airglow image data, Applied optics, 36, 7374–7385, https://doi.org/10.1364/AO.36.007374, 1997.

Gelaro, R., McCarty, W., Suárez, M. J., Todling, R., Molod, A., Takacs, L., Randles, C. A., Darmenov, A., Bosilovich, M. G., Reichle, R., et al.: The modern-era retrospective analysis for research and applications, version 2 (MERRA-2), Journal of Climate, 30, 5419–5454, https://doi.org/10.1175/JCLI-D-16-0758.1, 2017.

Giongo, G. A., Bageston, J. V., Figueiredo, C. A., Wrasse, C. M., Kam, H., Kim, Y. H., and Schuch, N. J.: Gravity Wave Investigations over Comandante Ferraz Antarctic Station in 2017: General Characteristics, Wind Filtering and Case Study, Atmosphere, 11, 880, https://doi.org/10.3390/atmos11080880, 2020.

Globo News: RS registra granizo e rajadas de vento de mais de 100 km/h, https://g1.globo.com/rs/rio-grande-do-sul/noticia/2019/10/02/rs-registra-granizo-e-rajadas-de-vento-de-mais-de-100-kmh.ghtml, 2019.

Gossard, E. E. and Hooke, W. H.: Waves in the atmosphere: atmospheric infrasound and gravity waves-their generation and propagation, Atmospheric Science, 2, 1975.

Griffin, S. M., Bedka, K. M., and Velden, C. S.: A method for calculating the height of overshooting convective cloud tops using satellite-based IR imager and CloudSat cloud profiling radar observations, Journal of Applied Meteorology and Climatology, 55, 479–491, https://doi.org/10.1175/JAMC-D-15-0170.1, 2016.

Heymsfield, G. M. and Blackmer Jr, R. H.: Satellite-observed characteristics of Midwest severe thunderstorm anvils, Monthly weather review, 116, 2200–2224, https://doi.org/https://doi.org/10.1175/1520-0493(1988)116<2200:SOCOMS>2.0.CO;2, 1988.

Jurković, P. M., Mahović, N. S., and Počakal, D.: Lightning, overshooting top and hail characteristics for strong convective storms in Central Europe, Atmospheric Research, 161, 153–168, https://doi.org/10.1016/j.atmosres.2015.03.020, 2015.

Kim, J. and Son, S.-W.: Tropical cold-point tropopause: Climatology, seasonal cycle, and intraseasonal variability derived from COSMIC GPS radio occultation measurements, Journal of Climate, 25, 5343–5360, https://doi.org/https://doi.org/10.1175/JCLI-D-11-00554.1, 2012.

Kim, J., Randel, W. J., and Birner, T.: Convectively driven tropopause-level cooling and its influences on stratospheric moisture, Journal of Geophysical Research: Atmospheres, 123, 590–606, https://doi.org/https://doi.org/10.1002/2017JD027080, 2018.

Lane, T. P., Reeder, M. J., and Clark, T. L.: Numerical modeling of gravity wave generation by deep tropical convection, Journal of the atmospheric sciences, 58, 1249–1274, https://doi.org/10.1175/1520-0469(2001)058<1249:NMOGWG>2.0.CO;2, 2001.

Lane, T. P., Reeder, M. J., and Guest, F. M.: Convectively generated gravity waves observed from radiosonde data taken during MCTEX, Quarterly Journal of the Royal Meteorological Society, 129, 1731–1740, https://doi.org/10.1256/qj.02.196, 2003.

Medeiros, A., Taylor, M. J., Takahashi, H., Batista, P., and Gobbi, D.: An investigation of gravity wave activity in the low-latitude upper mesosphere: Propagation direction and wind filtering, Journal of Geophysical Research: Atmospheres, 108, https://doi.org/https://doi.org/10.1029/2002JD002593, 2003.

Naccarato, K. P. and Pinto, J. O.: Improvements in the detection efficiency model for the Brazilian lightning detection network (BrasilDAT), Atmospheric Research, 91, 546–563, https://doi.org/10.1016/j.atmosres.2008.06.019, 2009.

Naccarato, K. P. and Pinto, J. O.: Lightning detection in Southeastern Brazil from the new Brazilian Total lightning network (BrasilDAT), in: 2012 International Conference on Lightning Protection (ICLP), pp. 1–9, IEEE, 2012.

Nappo, C. J.: An introduction to atmospheric gravity waves, Academic press, 2013.

Nyassor, P. K., Buriti, R. A., Paulino, I., Medeiros, A. F., Takahashi, H., Wrasse, C. M., and Gobbi, D.: Determination of gravity wave parameters in the airglow combining photometer and imager data, in: Annales Geophysicae, vol. 36, pp. 705–715, Copernicus GmbH, https://doi.org/10.5194/angeo-36-705-2018, 2018.

Nyassor, P. K., Wrasse, C. M., Gobbi, D., Paulino, I., Vadas, S. L., Naccarato, K. P., Takahashi, H., Bageston, J. V., Figueiredo, C. A. O. B., and Barros, D.: Case Studies on Concentric Gravity Waves Source Using Lightning Flash Rate, Brightness Temperature and Backward Ray Tracing at São Martinho da Serra (29.44°S, 53.82°W), Journal of Geophysical Research: Atmospheres, 126, e2020JD034 527, https://doi.org/https://doi.org/10.1029/2020JD034527, 2021.

Pasko, V. P., Yair, Y., and Kuo, C.-L.: Lightning related transient luminous events at high altitude in the Earth's atmosphere: Phenomenology, mechanisms and effects, Space science reviews, 168, 475–516, https://doi.org/https://DOI 10.1007/s11214-011-9813-9, 2012.

Pedoe, D.: Circles: a mathematical view, Cambridge University Press, 1995.

Picone, J., Hedin, A., Drob, D. P., and Aikin, A.: NRLMSISE-00 empirical model of the atmosphere: Statistical comparisons and scientific issues, Journal of Geophysical Research: Space Physics, 107, SIA–15, https://doi.org/10.1029/2002JA009430, 2002.

Press, W. H., Teukolsky, S. A., Vetterling, W. T., and Flannery, B. P.: Numerical recipes 3rd edition: The art of scientific computing, Cambridge university press, 2007.

São Sabbas, F. and Sentman, D.: Dynamical relationship of infrared cloudtop temperatures with occurrence rates of cloud-to-ground lightning
and sprites, Geophysical research letters, 30, https://doi.org/https://doi.org/10.1029/2002GL015382, 2003.

São Sabbas, F., Rampinelli, V., Santiago, J., Stamus, P., Vadas, S., Fritts, D., Taylor, M., Pautet, P., Dolif Neto, G., and Pinto, O.: Charac-
teristics of sprite and gravity wave convective sources present in satellite IR images during the SpreadFEx 2005 in Brazil, in: Annales
geophysicae, vol. 27, pp. 1279–1293, Copernicus GmbH, 2009.

São Sabbas, F., Taylor, M. J., Pautet, P.-D., Bailey, M., Cummer, S., Azambuja, R., Santiago, J., Thomas, J., Pinto, O., Solorzano, N., et al.:
Observations of prolific transient luminous event production above a mesoscale convective system in Argentina during the Sprite2006
Campaign in Brazil, Journal of Geophysical Research: Space Physics, 115, https://doi.org/https://doi.org/10.1029/2009JA014857, 2010.

São Sabbas, F., Souza, J., Guerra, E., Naccarato, K., Lambas, D., Rolim, J., Van Meer, H., Massini, J., Secanell, E., Villalobos, C., et al.:
TLEs Detected with LEONA Network during RELAMPAGO Campaign: Preliminary Results, in: AGU Fall Meeting Abstracts, vol. 2019,
pp. AE31B–3099, 2019.

Sentman, D., Wescott, E., Picard, R., Winick, J., Stenbaek-Nielsen, H., Dewan, E., Moudry, D., Sao Sabbas, F., Heavner, M., and Morrill,
J.: Simultaneous observations of mesospheric gravity waves and sprites generated by a midwestern thunderstorm, Journal of Atmospheric
and Solar-Terrestrial Physics, 65, 537–550, https://doi.org/10.1016/S1364-6826(02)00328-0, 2003.

Sherwood, S. C., Horinouchi, T., and Zeleznik, H. A.: Convective impact on temperatures observed near the tropical tropopause, Journal of
the atmospheric sciences, 60, 1847–1856, https://doi.org/https://doi.org/10.1175/1520-0469(2003)060<1847:CIOTON>2.0.CO;2, 2003.

Takahashi, H., Wrasse, C. M., Figueiredo, C. A. O. B., Barros, D., Abdu, M. A., Otsuka, Y., and Shiokawa, K.: Equatorial plasma bubble
seeding by MSTIDs in the ionosphere, Progress in Earth and Planetary Science, 5, 1–13, https://doi.org/https://doi.org/10.1186/s40645-
018-0189-2, 2018.

Taylor, M. J., Ryan, E., Tuan, T., and Edwards, R.: Evidence of preferential directions for gravity wave propagation due to wind filtering in
the middle atmosphere, Journal of Geophysical Research: Space Physics, 98, 6047–6057, https://doi.org/10.1029/92JA02604, 1993.

Torrence, C. and Compo, G. P.: A practical guide to wavelet analysis, Bulletin of the American Meteorological society, 79, 61–78,
https://doi.org/10.1175/1520-0477(1998)079<0061:APGTWA>2.0.CO;2, 1998.

Vadas, S. L.: Horizontal and vertical propagation and dissipation of gravity waves in the thermosphere from lower atmospheric and thermo-
spheric sources, Journal of Geophysical Research: Space Physics, 112, https://doi.org/10.1029/2006JA011845, 2007.

Vadas, S. L. and Fritts, D.: Reconstruction of the gravity wave field from convective plumes via ray tracing, in: Annales geophysicae:
atmospheres, hydrospheres and space sciences, vol. 27, p. 147, https://doi.org/10.5194/angeo-27-147-2009, 2009.

Vadas, S. L. and Liu, H.-l.: Generation of large-scale gravity waves and neutral winds in the thermosphere from the dissipation of convectively
generated gravity waves, Journal of Geophysical Research: Space Physics, 114, https://doi.org/10.1029/2009JA014108, 2009.

Vadas, S. L., Taylor, M. J., Pautet, P.-D., Stamus, P., Fritts, D. C., Liu, H.-L., São Sabbos, F., Batista, V., Takahashi, H., and Rampinelli,
V.: Convection: the likely source of the medium-scale gravity waves observed in the OH airglow layer near Brasilia, Brazil, during the
SpreadFEx campaign, in: Annales Geophysicae, vol. 27, p. 231, European Geosciences Union, https://doi.org/10.5194/angeo-27-231-
2009, 2009a.

Vadas, S. L., Yue, J., She, C.-Y., Stamus, P. A., and Liu, A. Z.: A model study of the effects of winds on concentric rings of
gravity waves from a convective plume near Fort Collins on 11 May 2004, Journal of Geophysical Research: Atmospheres, 114,
https://doi.org/10.1029/2008JD010753, 2009b.

Vadas, S. L., Yue, J., and Nakamura, T.: Mesospheric concentric gravity waves generated by multiple convective storms over the North
American Great Plain, Journal of Geophysical Research: Atmospheres, 117, https://doi.org/10.1029/2011JD017025, 2012.

Wen, Y., Zhang, Q., Gao, H., Xu, J., and Li, Q.: A case study of the stratospheric and mesospheric concentric gravity waves excited by thunderstorm in Northern China, Atmosphere, 9, 489, https://doi.org/https://doi.org/10.3390/atmos9120489, 2018.

Wrasse, C. M., Nakamura, T., Tsuda, T., Takahashi, H., Gobbi, D., Medeiros, A. F., and Taylor, M. J.: Atmospheric wind effects on the gravity
700 wave propagation observed at 22.7°S-Brazil, Advances in Space Research, 32, 819–824, https://doi.org/10.1016/S0273-1177(03)00413-7, 2003.

Wrasse, C. M., Takahashi, H., Medeiros, A. F., Lima, L. M., Taylor, M. J., Gobbi, D., and Fechine, J.: Determinaçao dos parâmetros de ondas de gravidade através da análise espectral de imagens de aeroluminescência, Revista Brasileira de Geofísica, 25, 257–265, https://doi.org/10.1590/S0102-261X2007000300003, 2007.

705 Xian, T. and Homeyer, C. R.: Global tropopause altitudes in radiosondes and reanalyses, Atmospheric Chemistry and Physics, 19, 5661–5678, https://doi.org/https://doi.org/10.5194/acp-19-5661-2019, 2019.

Xu, J., Li, Q., Yue, J., Hoffmann, L., Straka, W. C., Wang, C., Liu, M., Yuan, W., Han, S., Miller, S. D., et al.: Concentric gravity waves over northern China observed by an airglow imager network and satellites, Journal of Geophysical Research: Atmospheres, 120, https://doi.org/10.1002/2015JD023786, 2015.

710 Yiğit, E. and Medvedev, A. S.: Heating and cooling of the thermosphere by internal gravity waves, Geophysical Research Letters, 36, 2009.

Yiğit, E., Medvedev, A. S., and Ern, M.: Effects of latitude-dependent gravity wave source variations on the middle and upper atmosphere, Frontiers in Astronomy and Space Sciences, p. 117, 2021.

Yue, J., Vadas, S. L., She, C.-Y., Nakamura, T., Reising, S. C., Liu, H.-L., Stamus, P., Krueger, D. A., Lyons, W., and Li, T.: Concentric gravity waves in the mesosphere generated by deep convective plumes in the lower atmosphere near Fort Collins, Colorado, Journal of
715 Geophysical Research: Atmospheres, 114, https://doi.org/10.1029/2008JD011244, 2009.

Yue, J., Hoffmann, L., and Joan Alexander, M. J.: Simultaneous observations of convective gravity waves from a ground-based airglow imager and the AIRS satellite experiment, Journal of Geophysical Research: Atmospheres, 118, 3178–3191, https://doi.org/10.1002/jgrd.50341, 2013.

Yue, J., Miller, S. D., Hoffmann, L., and Straka, W. C.: Stratospheric and mesospheric concentric gravity waves over tropical cy-
720 clone Mahasen: Joint AIRS and VIIRS satellite observations, Journal of atmospheric and solar-terrestrial physics, 119, 83–90, https://doi.org/10.1016/j.jastp.2014.07.003, 2014.